NOAA Technical Memorandum ERL SEL-48

DEPARTMENT OF COMMERCE
UNITED STATES OF AMERICA

SOLAR X-RAY MEASUREMENTS FROM SMS-1, SMS-2, AND GOES-1
INFORMATION FOR DATA USERS

R. F. Donnelly
R. N. Grubb
F. C. Cowley

Space Environment Laboratory
Boulder, Colorado
June 1977

---

noaa NATIONAL OCEANIC AND ATMOSPHERIC ADMINISTRATION / Environmental Research Laboratories

NOAA Technical Memorandum ERL SEL-48

SOLAR X-RAY MEASUREMENTS FROM SMS-1, SMS-2, AND GOES-1 INFORMATION FOR DATA USERS

R. F. Donnelly
R. N. Grubb
F. C. Cowley

Space Environment Laboratory
Boulder, Colorado
June 1977

UNITED STATES
DEPARTMENT OF COMMERCE
Juanita M. Kreps, Secretary

NATIONAL OCEANIC AND
ATMOSPHERIC ADMINISTRATION
Robert M. White, Administrator

Environmental Research
Laboratories
Wilmot N. Hess, Director

NOTICE

The Environmental Research Laboratories do not approve, recommend, or endorse any proprietary product or proprietary material mentioned in this publication. No reference shall be made to the Environmental Research Laboratories or to this publication furnished by the Environmental Research Laboratories in any advertising or sales promotion which would indicate or imply that the Environmental Research Laboratories approve, recommend, or endorse any proprietary product or proprietary material mentioned herein, or which has as its purpose an intent to cause directly or indirectly the advertised product to be used or purchased because of this Environmental Research Laboratories publication.

TABLE OF CONTENTS

LIST OF TABLES

LIST OF TABLES (Cont.)

LIST OF FIGURES

LIST OF FIGURES (Cont.)

SOLAR X-RAY MEASUREMENTS FROM SMS-1, SMS-2, and GOES-1

INFORMATION FOR DATA USERS

R. F. Donnelly, R. N. Grubb and F. C. Cowley
Space Environment Laboratory
NOAA Environmental Research Laboratories
Boulder, Colorado 80302

Solar broadband X-ray measurements in the $\frac{1}{2}$-4 A and 1-8 A ranges from the SMS and GOES satellites are described, including the following: time coverage, detector transfer functions, solar spectra sensitivity, in-flight calibrations, and intercomparisons of concurrent measurements from the SMS-1, SMS-2, and GOES-1 satellites.

1. X-RAY MEASUREMENTS OF THE SPACE ENVIRONMENT MONITORING SYSTEM

The Synchronous Meteorological Satellites (SMS) and the Geostationary Operational Environmental Satellites (GOES) include the Space Environment Monitoring System (SEMS), which consists of three types of measurements: energetic particles, magnetic field, and solar X-rays. The X-ray measurements are described here to provide technical information to those using these data. The SMS and GOES solar X-ray measurements are available in real time and in five-minute averages for the preceding 32-day period from SELDADs (Space Environment Laboratory Data Acquisition and Display System) through the Space Environment Service Center, NOAA, ERL, Boulder, Colorado 80302 (Williams, 1976). Older data are available from World Data Center A for Solar Terrestrial Physics, NOAA Environmental Data Service, Boulder, Colorado 80302.

The SMS and GOES satellites are geostationary and spaced in longitude over the American hemisphere. The satellites spin at approximately 100 rpm. The spin axis is nearly perpendicular to the equatorial plane. The X-ray detectors scan the Sun once per satellite rotation (∿0.6 sec.). The data are filtered and a sample is transmitted to the ground about once every three seconds. A stepping motor adjusts the elevation angle of the detectors with respect to the plane perpendicular to the spin axis. This angle is adjusted slowly during the year to correct for the seasonal variations of the angle between the Earth-Sun line and the equatorial plane.

Because these satellites are in the high-energy particle environment of the magnetosphere, a magnetic broom and baffle collimator are used to reduce errors in the X-ray measurements caused by energetic particles. The detector response to particles is sampled just prior to each observation of the solar X-ray flux. The X-ray measurement is made by subtracting this background level from the total response when the Sun is being viewed. This subtraction is done on the satellite, and the difference is telemetered. Several measures of the background noise are also telemetered (see sect. 4).

The X-ray detectors are simple ion chambers as described in Table 1.1. Two channels are used, namely $\frac{1}{2}$-4 A and 1-8 A. These wavelength bands were picked because full disk measurements at those wavelengths provide extremely sensitive data for the early detection of solar flares (Donnelly, 1968) and because the measured fluxes are directly applicable for computing D-region sudden ionospheric disturbances (SID), e.g., short-wave fadeouts (SWF). In order to provide a large dynamic range and high intensity resolution, the electronics that amplify the weak current output of the ion chambers use four gain ranges, where adjacent ranges overlap slightly. The instrument automatically switches from one range to another according to the X-ray flux intensity. The ion-chamber output level where the electrometer switches to a lower gain range is offset with respect to the level where the system will switch back to the higher gain range in order to avoid repetitive switching between ranges. Systematic errors occur in the data for each switch in ranges because of electronic switching transients (see sect. 4). The overall SEMS instruments are described in greater detail by Grubb (1975).

Table 1.1 General Characteristics of SMS/GOES X-Ray Ion Chambers

		Wavelength Band	
		$\frac{1}{2}$-4 A	1-8 A
Beryllium Filter Window			
Thickness, m		5×10^{-4}	5×10^{-5}
Area, m^2		5.8×10^{-4}	1.9×10^{-4}
Weight, kg/m^2:	SMS-1	0.939	0.0872
	SMS-2	0.929	0.0891
(including UV filter)	GOES-1	0.952	0.1080
Filler Gas		Xenon	Argon
Gas Pressure, mm Hg		180	800
Intensity Ranges	Range No.		
The soft X-ray	1	$\Phi \leq a \times 10^{-7}$	$\Phi \leq f \times 10^{-6}$
flux units are	2	$a \times 10^{-7} < \Phi \leq b \times 10^{-6}$	$f \times 10^{-6} < \Phi \leq g \times 10^{-5}$
Wm^{-2} at Earth	3	$b \times 10^{-6} < \Phi \leq c \times 10^{-5}$	$g \times 10^{-5} < \Phi \leq h \times 10^{-4}$
where 1 Wm^{-2} =	4	$c \times 10^{-5} < \Phi \leq d \times 10^{-4}$	$h \times 10^{-4} < \Phi \lesssim \times 10^{-3}$
10^3 ergs cm^{-2} sec^{-1}.			

	a	b	c	d	f	g	h
SMS-1	1.4	1.4	1.6	1.6	1.3	1.3	1.4
SMS-2	1.7	1.6	1.6	∿1.5	1.3	1.3	1.4
GOES-1	1.6	1.5	1.5	∿1.5	1.2	1.2	1.2

Intensity Resolution: ∿ 0.2% to 0.3% of the maximum flux of a range.

Spatial Resolution: none, collimated to view full disk.

Sample Rate: every 3 sec

Wavelength Resolution: none within the 1/2-4 A and 1-8 A bands.

2. TIME COVERAGE OF MEASUREMENTS

Table 2.1 lists the dates when the X-ray data from SMS-1, SMS-2, and GOES-1 were received in Boulder. Two telemetry receiving systems are available in Boulder, so only two of the three satellites are monitored. X-ray data are now available in real time in the NOAA/SEL Space Environment Service Center essentially all the time (>99% of the time). The percentage of data available on archival magnetic tapes is less because of occasional failures of on-line computer systems. Full-disk solar X-rays are not measured by a particular satellite at certain times for the following reasons: eclipse of the Sun by the Earth near equinox, calibrations, eclipse of the Sun by the Moon, dwell-mode telemetry, and occasional telemetry problems. Dwell mode telemetry is a rare case in which a designated measurement is sampled and telemetered 20 times per second, while other measurements are not telemetered, i.e., the telemetry "dwells" on a particular measurement. The satellites (SMS-1, SMS-2, and GOES-1) are sufficiently separated in longitude that their eclipse periods do not overlap. Calibrations and dwell-mode telemetry are performed at different times on the two monitored satellites to obtain full-time X-ray measurements from the pair of satellites.

Eclipse of the Sun at the satellite by the Earth has a maximum duration of about 1.2 hours at equinox centered on midnight for the longitude of the satellite. The duration of the eclipse is progressively shorter for dates further from equinox, as shown in Figure 2.1, until no eclipse occurs for dates more than 24 days from equinox. Now that several satellites are in operation, the experiments are decommissioned for a larger block of time near the eclipse to simplify scheduling. Eclipses of the Sun by the Moon as viewed by the SMS and GOES are fairly rare. Table 2.2 lists these events through 1976. In-flight calibrations of the X-ray instrument electronics were made twice per day and lasted less than ten minutes. In 1976, calibrations were usually made at about 0350 UT and 1600 UT for GOES-1, 1110 and 2130 UT for SMS-2, and 0450 and 1650 UT for SMS-1. Starting in January 1977, calibrations are being made once per week on Mondays.

Table 2.1. Dates of SMS/GOES Solar X-Ray Monitoring

Satellite	Launch Date	Approximate Geostationary Longitude*	X-Ray Data Monitored in Boulder**
SMS-1	May 16, 1974	45°W June-Sept. 1974 75°W Nov. 1974-Dec. 1975 105°W Feb. 1976 - present	May 23, 1974† to Jan. 8, 1976 May 18, 1976 to Aug. 16, 1976 May 9, 1977 to present
SMS-2	Feb. 6, 1975	115°W March-Nov. 1975 135°W Jan. 1976 - present	Feb. 10, 1975 to May 18, 1976 Aug. 16, 1976 to May 9, 1977
GOES-1	Oct. 16, 1975	55°W Nov. 1975 75°W Dec. 1975 - present	Jan. 8, 1976 to present

---

*The satellites were moved to different longitudes on several occasions.

**Only two of these satellites can be monitored in Boulder at one time because of ground-station receiving equipment limitations. No X-ray instrument has yet failed or is known to have suffered significant degradation.

†Archive data start July 1, 1974.

*Table 2.2. Eclipses of the Sun by the Moon at the SMS/GOES Satellites**

Satellite	Date	Predicted Approximate Eclipse Times Start	Maximum	End	Maximum Photospheric Obscuration
SMS-1	November 14, 1974	0034	0400	0416	78%
SMS-2	December 2, 1975	1614	1652	1725	94%
SMS-2	November 22, 1976	0005	0030	0057	18%
GOES-1	November 21, 1976	1731	1759	1827	77%

---

*Data provided by Mr. R. J. Went of NOAA, NESS, Suitland, Maryland.

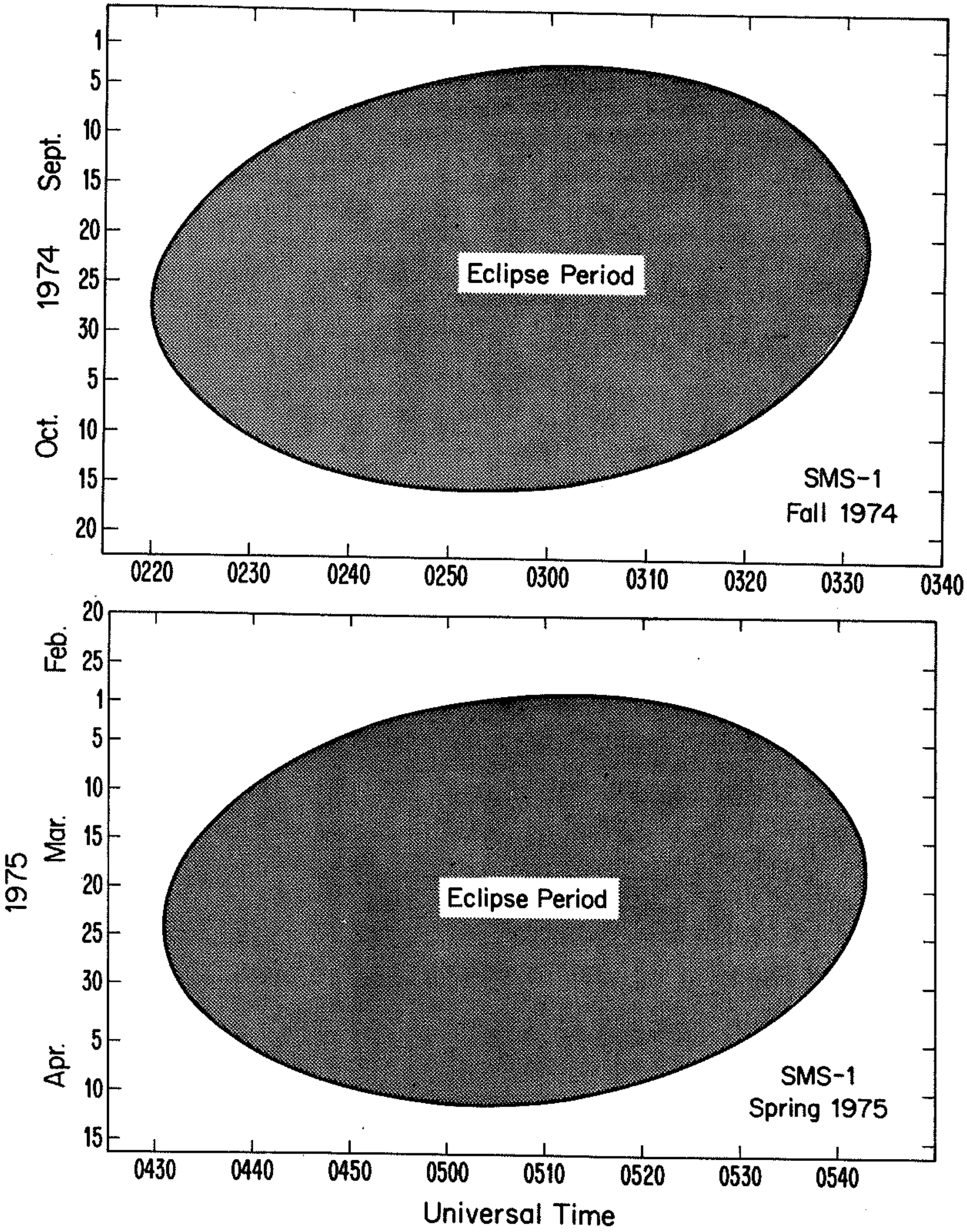

Figure 2.1. Eclipse of the Sun by Earth at SMS-1.

3. TRANSFER FUNCTION

3.1 Theoretical and Calibration Results for G(λ)

The time-varying current output I(t) of the ion chamber, which is induced by the incident X-ray energy flux $\phi(\mathrm{W\ m^{-2} A^{-1}})$ as a function of wavelength λ, can be expressed in terms of a transfer function G(λ) by

$$I(t) = C \int_0^\infty G(\lambda)\phi(\lambda,t)d\lambda \quad , \qquad (3.1)$$

where C accounts for the attenuation from the collimator ($C_{max} = 1$ for 1-8 A and $C_{max} = 0.9333$ for $\frac{1}{2}$-4 A) and, of course, G(λ) depends on the filter window transmission, window area, absorption of X-rays by the filler gas, etc. The results of theoretical calculations and laboratory measurements of G(λ) for the SMS-1 satellite of Unzicker and Donnelly (1974) are given in Table 3.1 and shown in Figure 3.1. Similar theoretical calculations using the measured window weights for SMS-2 and GOES-1 are also given in Table 3.1, where these latter results do not include revisions to fit the theoretical results to calibration measurements. Although the ion chambers originally intended for use on SMS-2 and GOES-1 were calibrated, those detectors failed before launch and were replaced by ion chambers that were uncalibrated, but were nearly identical.

3.2 Wavelength Averaged Transfer Function $\overline{G}$

The telemetry output, which is proportional to I, is used to deduce the soft X-ray flux Φ in the wavelength range λ_1 to λ_2, from

$$\Phi(\lambda_1-\lambda_2,\ t) = \frac{1}{\overline{G}(\lambda_1 - \lambda_2)} \frac{I(t)}{C} \qquad (3.2)$$

Table 3.1. G(λ) Ion Chamber Transfer Functions

$\frac{1}{2}$-4 A Channels

Wavelength λ (A)	Satellite SMS-1	SMS-2	GOES-1
0.1	1.56×10^{-7}	1.62×10^{-7}	1.62×10^{-7}
0.2	6.01×10^{-7}	6.22×10^{-7}	6.21×10^{-7}
0.3	1.33×10^{-6}	1.38×10^{-6}	1.38×10^{-6}
0.4	9.77×10^{-7}	1.01×10^{-6}	1.01×10^{-6}
0.5	1.75×10^{-6}	1.80×10^{-6}	1.80×10^{-6}
0.6	2.78×10^{-6}	2.87×10^{-6}	2.87×10^{-6}
0.7	3.90×10^{-6}	4.03×10^{-6}	4.03×10^{-6}
0.8	5.43×10^{-6}	5.61×10^{-6}	5.61×10^{-6}
0.9	7.48×10^{-6}	7.74×10^{-6}	7.73×10^{-6}
1.0	8.94×10^{-6}	9.25×10^{-6}	9.24×10^{-6}
1.1	1.06×10^{-5}	1.10×10^{-5}	1.10×10^{-5}
1.2	1.25×10^{-5}	1.29×10^{-5}	1.29×10^{-5}
1.3	1.42×10^{-5}	1.47×10^{-5}	1.47×10^{-5}
1.4	1.57×10^{-5}	1.63×10^{-5}	1.63×10^{-5}
1.5	1.66×10^{-5}	1.72×10^{-5}	1.71×10^{-5}
1.6	1.75×10^{-5}	1.81×10^{-5}	1.80×10^{-5}
1.7	1.80×10^{-5}	1.86×10^{-5}	1.86×10^{-5}
1.8	1.83×10^{-5}	1.90×10^{-5}	1.89×10^{-5}
1.9	1.84×10^{-5}	1.91×10^{-5}	1.90×10^{-5}
2.0	1.83×10^{-5}	1.89×10^{-5}	1.88×10^{-5}
2.1	1.79×10^{-5}	1.86×10^{-5}	1.85×10^{-5}
2.2	1.74×10^{-5}	1.81×10^{-5}	1.80×10^{-5}
2.3	1.66×10^{-5}	1.72×10^{-5}	1.71×10^{-5}
2.4	1.59×10^{-5}	1.65×10^{-5}	1.64×10^{-5}
2.5	1.47×10^{-5}	1.53×10^{-5}	1.51×10^{-5}
2.6	1.10×10^{-5}	1.14×10^{-5}	1.13×10^{-5}
2.7	1.09×10^{-5}	1.14×10^{-5}	1.12×10^{-5}
2.8	1.07×10^{-5}	1.11×10^{-5}	1.10×10^{-5}
2.9	1.05×10^{-5}	1.09×10^{-5}	1.07×10^{-5}
3.0	1.01×10^{-5}	1.05×10^{-5}	1.04×10^{-5}
3.1	9.68×10^{-6}	1.01×10^{-5}	9.89×10^{-6}
3.2	9.17×10^{-6}	9.56×10^{-6}	9.36×10^{-6}
3.3	8.60×10^{-6}	8.98×10^{-6}	8.77×10^{-6}
3.4	8.00×10^{-6}	8.35×10^{-6}	8.14×10^{-6}
3.5	7.38×10^{-6}	7.71×10^{-6}	7.50×10^{-6}
3.6	6.68×10^{-6}	6.99×10^{-6}	6.68×10^{-6}
3.8	5.48×10^{-6}	5.75×10^{-6}	5.54×10^{-6}
4.0	4.35×10^{-6}	4.57×10^{-6}	4.38×10^{-6}
4.2	3.23×10^{-6}	3.41×10^{-6}	3.25×10^{-6}
4.4	2.39×10^{-6}	2.53×10^{-6}	2.39×10^{-6}
4.6	1.71×10^{-6}	1.82×10^{-6}	1.70×10^{-6}
4.8	1.19×10^{-6}	1.26×10^{-6}	1.17×10^{-6}
5.0	7.94×10^{-7}	8.50×10^{-7}	7.81×10^{-7}
5.5	2.41×10^{-7}	2.62×10^{-7}	2.33×10^{-7}
6.0	5.70×10^{-8}	6.26×10^{-8}	5.39×10^{-8}
7.0	1.46×10^{-9}	1.67×10^{-9}	1.31×10^{-9}
8.0	1×10^{-11}	1×10^{-11}	1×10^{-11}
K-Shell Edge			
0.3584^{-}	1.65×10^{-6}	1.56×10^{-6}	1.79×10^{-6}
0.3584^{+}	7.39×10^{-7}	7.89×10^{-7}	7.89×10^{-7}
L-Shell Edge			
2.587^{-}	1.41×10^{-5}	1.47×10^{-5}	1.45×10^{-5}
2.587^{+}	1.10×10^{-5}	1.14×10^{-5}	1.13×10^{-5}

1-8 A Channels

Wavelength λ (A)	Satellite SMS-1	SMS-2	GOES-1
0.2	1.68×10^{-8}	2.10×10^{-8}	2.10×10^{-8}
0.4	1.12×10^{-7}	1.40×10^{-7}	1.40×10^{-7}
0.6	3.34×10^{-7}	4.18×10^{-7}	4.18×10^{-7}
0.8	7.08×10^{-7}	8.87×10^{-7}	8.87×10^{-7}
1.0	1.23×10^{-6}	1.55×10^{-6}	1.54×10^{-6}
1.2	1.88×10^{-6}	2.35×10^{-6}	2.34×10^{-6}
1.4	2.59×10^{-6}	3.24×10^{-6}	3.24×10^{-6}
1.6	3.29×10^{-6}	4.12×10^{-6}	4.11×10^{-6}
1.8	3.90×10^{-6}	4.89×10^{-6}	4.87×10^{-6}
2.0	4.40×10^{-6}	5.51×10^{-6}	5.49×10^{-6}
2.2	4.79×10^{-6}	5.95×10^{-6}	5.92×10^{-6}
2.4	4.97×10^{-6}	6.22×10^{-6}	6.18×10^{-6}
2.6	5.08×10^{-6}	6.35×10^{-6}	6.29×10^{-6}
2.8	5.10×10^{-6}	6.38×10^{-6}	6.31×10^{-6}
3.0	5.07×10^{-6}	6.34×10^{-6}	6.25×10^{-6}
3.2	5.00×10^{-6}	6.25×10^{-6}	6.14×10^{-6}
3.4	4.91×10^{-6}	6.14×10^{-6}	6.01×10^{-6}
3.6	4.80×10^{-6}	6.00×10^{-6}	5.85×10^{-6}
3.8	4.69×10^{-6}	5.85×10^{-6}	5.68×10^{-6}
4.0	3.35×10^{-6}	4.16×10^{-6}	4.02×10^{-6}
4.2	3.45×10^{-6}	4.30×10^{-6}	4.12×10^{-6}
4.4	3.53×10^{-6}	4.40×10^{-6}	4.20×10^{-6}
4.6	3.60×10^{-6}	4.48×10^{-6}	4.24×10^{-6}
4.8	3.62×10^{-6}	4.50×10^{-6}	4.24×10^{-6}
5.0	3.61×10^{-6}	4.49×10^{-6}	4.19×10^{-6}
5.2	3.56×10^{-6}	4.42×10^{-6}	4.09×10^{-6}
5.4	3.49×10^{-6}	4.33×10^{-6}	3.96×10^{-6}
5.6	3.39×10^{-6}	4.20×10^{-6}	3.81×10^{-6}
5.8	3.27×10^{-6}	4.05×10^{-6}	3.62×10^{-6}
6.0	3.13×10^{-6}	3.87×10^{-6}	3.42×10^{-6}
6.2	2.98×10^{-6}	3.67×10^{-6}	3.21×10^{-6}
6.4	2.81×10^{-6}	3.47×10^{-6}	2.99×10^{-6}
6.8	2.47×10^{-6}	3.04×10^{-6}	2.54×10^{-6}
7.2	2.10×10^{-6}	2.57×10^{-6}	2.07×10^{-6}
7.6	1.76×10^{-6}	2.15×10^{-6}	1.66×10^{-6}
8.0	1.45×10^{-6}	1.77×10^{-6}	1.31×10^{-6}
8.4	1.16×10^{-6}	1.40×10^{-6}	9.92×10^{-7}
8.8	9.07×10^{-7}	1.09×10^{-6}	7.32×10^{-7}
9.2	6.96×10^{-7}	8.32×10^{-7}	5.27×10^{-7}
9.6	5.20×10^{-7}	6.18×10^{-7}	3.68×10^{-7}
10.0	3.80×10^{-7}	4.48×10^{-7}	2.49×10^{-7}
10.4	2.69×10^{-7}	3.15×10^{-7}	1.63×10^{-7}
10.8	1.85×10^{-7}	2.15×10^{-7}	1.02×10^{-7}
11.2	1.24×10^{-7}	1.43×10^{-7}	6.24×10^{-8}
11.6	8.13×10^{-8}	9.28×10^{-8}	3.69×10^{-8}
12.0	5.16×10^{-8}	5.83×10^{-8}	2.10×10^{-8}
13.0	1.39×10^{-8}	1.53×10^{-8}	4.16×10^{-9}
14.0	3.23×10^{-9}	3.43×10^{-9}	6.8×10^{-10}
15.0	6.07×10^{-10}	6.2×10^{-10}	9.0×10^{-11}
16.0	8.79×10^{-11}	9×10^{-11}	1.0×10^{-11}
K-Shell Edge			
3.87^{-}	4.65×10^{-6}	5.81×10^{-6}	5.63×10^{-6}
3.87^{+}	3.24×10^{-6}	4.05×10^{-6}	3.92×10^{-6}

Note: The units of G(λ) are amp $\text{watt}^{-1}\ \text{m}^{2}$, where 1 $\text{watt m}^{-2} = 10^{3}$ $\text{ergs cm}^{-2}\ \text{sec}^{-1}$. These G(λ) results include corrections for loss of fluorescence radiation. The SMS-1 results include a least squares difference fit to the measured G(λ) values using a correction factor constant with wavelength.

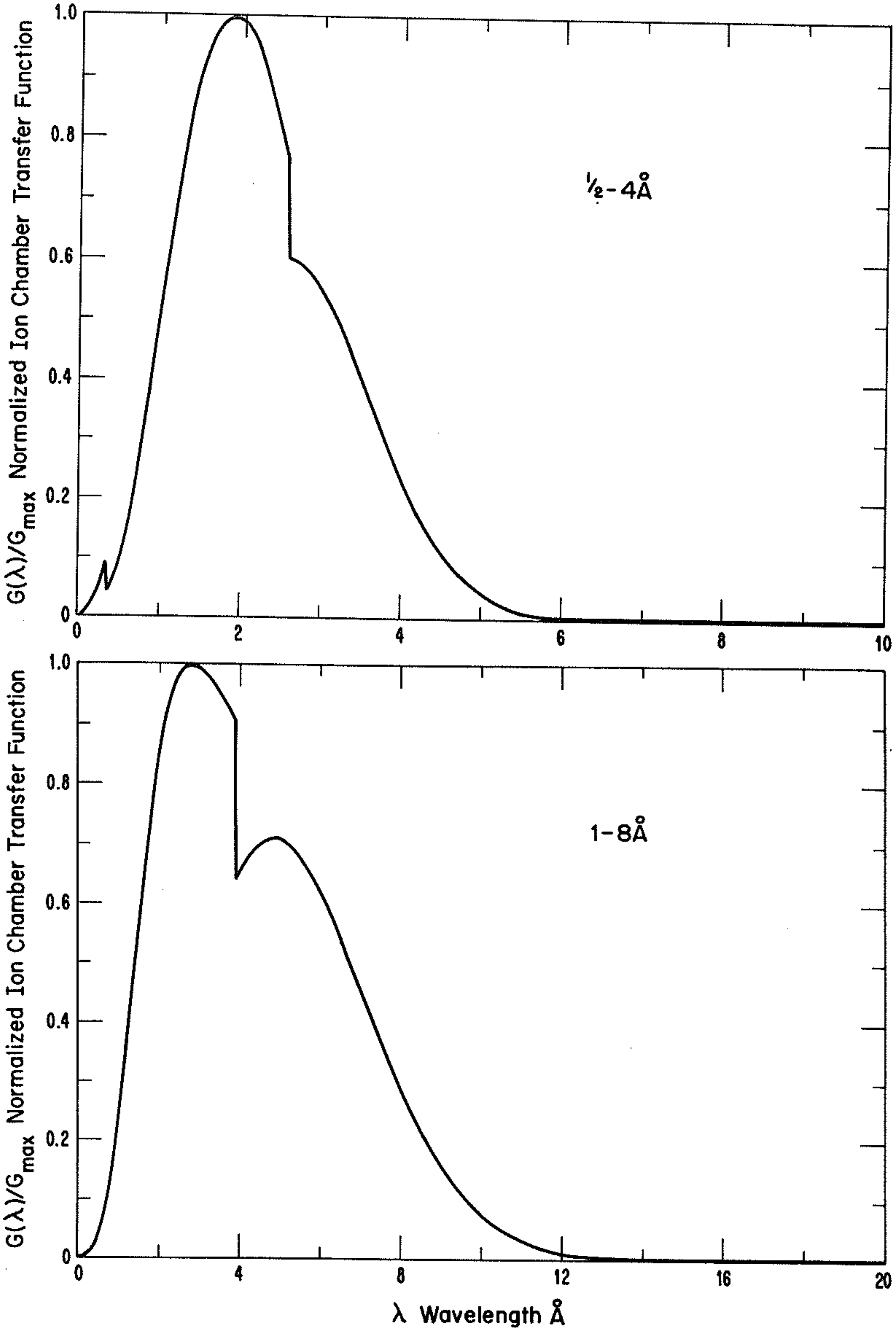

Figure 3.1. Relative wavelength dependence of SMS-1 ion chambers.

where $\overline{G}$, λ_1, and λ_2 are picked so as to give Φ results as accurate as possible. $\overline{G}$ is computed from

$$\overline{G}(\lambda_1 - \lambda_2) = \frac{\int_0^\infty G(\lambda)\ \phi(\lambda)\ d\lambda}{\int_{\lambda_1}^{\lambda_2} \phi\ (\lambda)\ \ d\lambda} \qquad (3.3)$$

The important assumption in evaluating (3.3) is to use $\phi(\lambda)$ with a spectral variation like that of the solar spectrum. This is complicated by the fact solar spectra vary with solar activity and during solar flares. Furthermore, although solar X-ray measurements with high wavelength resolution have been used to identify emission lines and to measure line ratios, no high-resolution measurements of <u>absolute</u> flux over the <u>whole</u> wavelength range important to the SMS-1 detectors (0.1 -20 A) have yet been published. Walker et al. (1974) have published absolute flux values for quiet-sun and post-flare conditions, but only for wavelengths longer than $3\frac{1}{2}$ A.

Early estimates of $\phi(\lambda)/\phi_{max}$ (Kreplin et al., 1976) assumed the solar spectrum was approximately like blackbody radiation with an effective temperature similar to coronal emissions like the spectra in figure 3.2. Figure 3.3 shows $G(1\text{-}8\ A,\lambda)\phi(\lambda)$ for the blackbody spectra in figure 3.2. Figure 3.4 shows similar results for the $\frac{1}{2}$-4 A ion chamber. Note that most of the 1-8 A ion chamber response comes from the 6-10 A radiation for a blackbody spectrum with a source temperature (T_s) of $2\text{x}10^6$K, and the 2-5 A radiation contributes most of the response when $T_s = 10^7$K. Solar spectra do not decrease with increasing wavelength in the 1-10 A range, except for emission lines and recombination edges, so the results in figures 3.2-3.4 are of interest primarily because of the historical use of blackbody spectra. Figure 3.5 shows isothermal free-free spectra (Tucker and Koren, 1971), which are slightly more realistic than blackbody spectra, but still lack emission lines. Compared with the blackbody spectra for the same source temperatures, the free-free spectra peak at longer wavelengths and decrease less with increasing wavelength at long wavelengths.

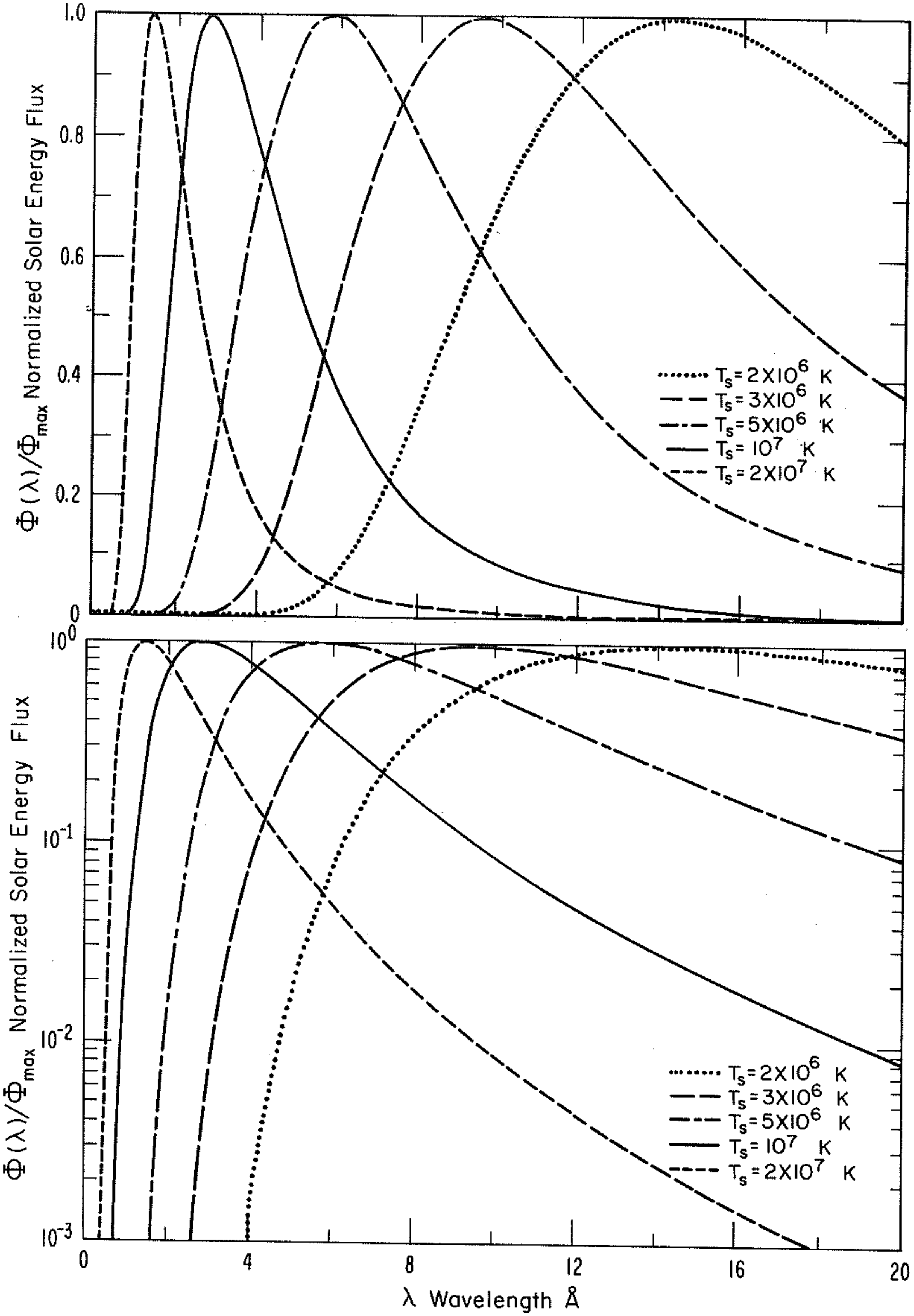

Figure 3.2. Normalized blackbody spectra.

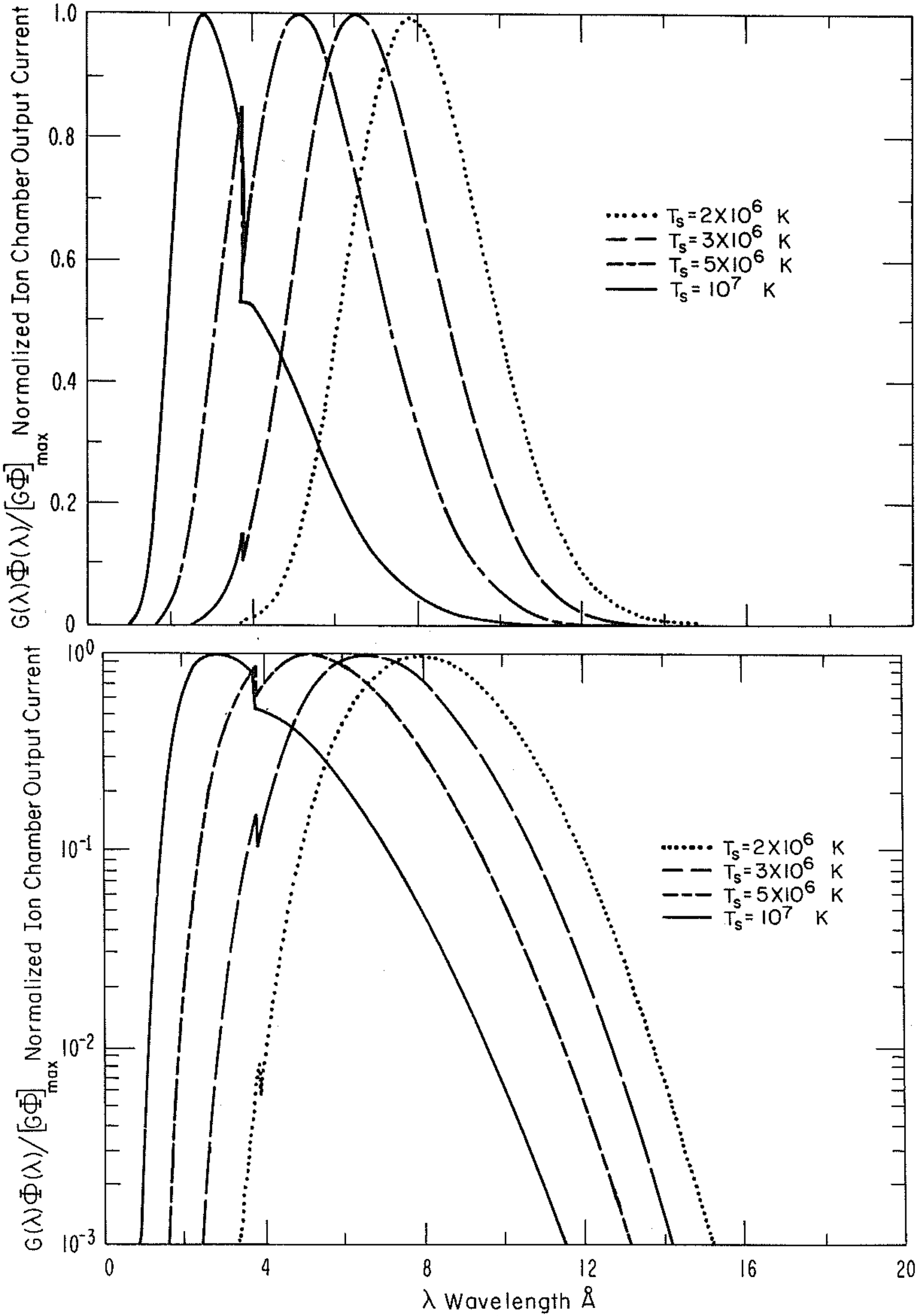

Figure 3.3. The 1-8A ion chamber response to blackbody spectra.

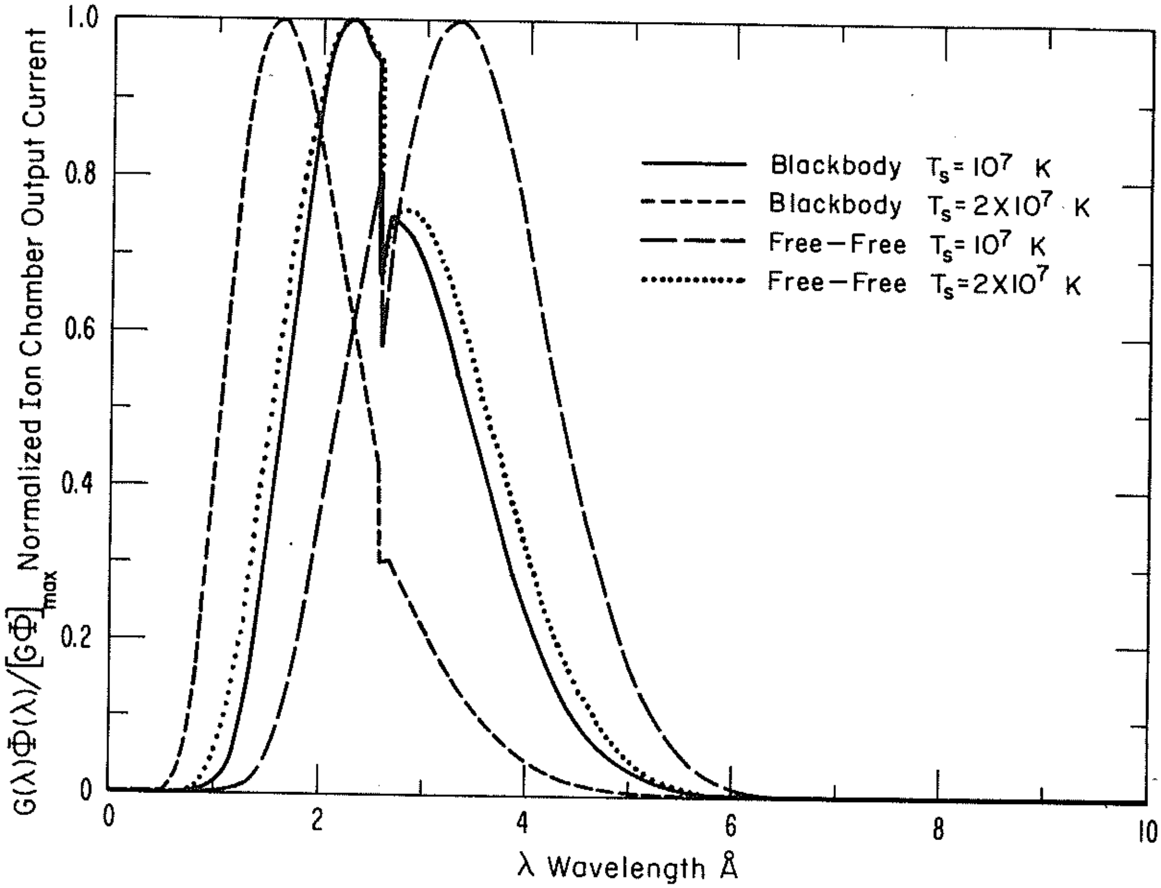

Figure 3.4. The 1/2-4 A ion chamber response to isothermal blackbody and free-free spectra.

Consequently the ion-chamber response is dominated by longer wavelengths for free-free spectra than for blackbody spectra, as can be seen by comparing figure 3.6 with figure 3.3, or by comparing the free-free and blackbody curves in figure 3.4.

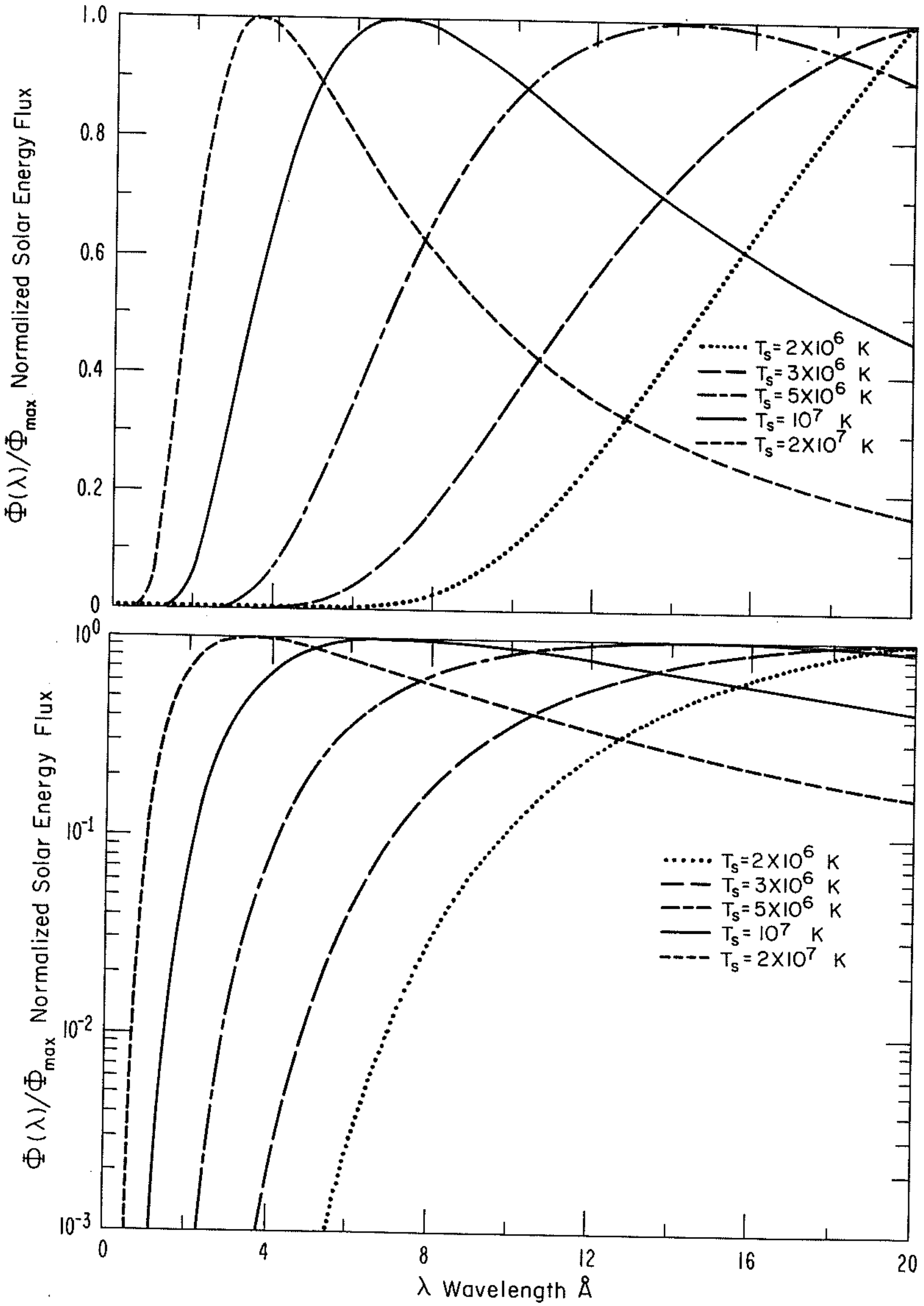

Figure 3.5. Isothermal free-free spectra.

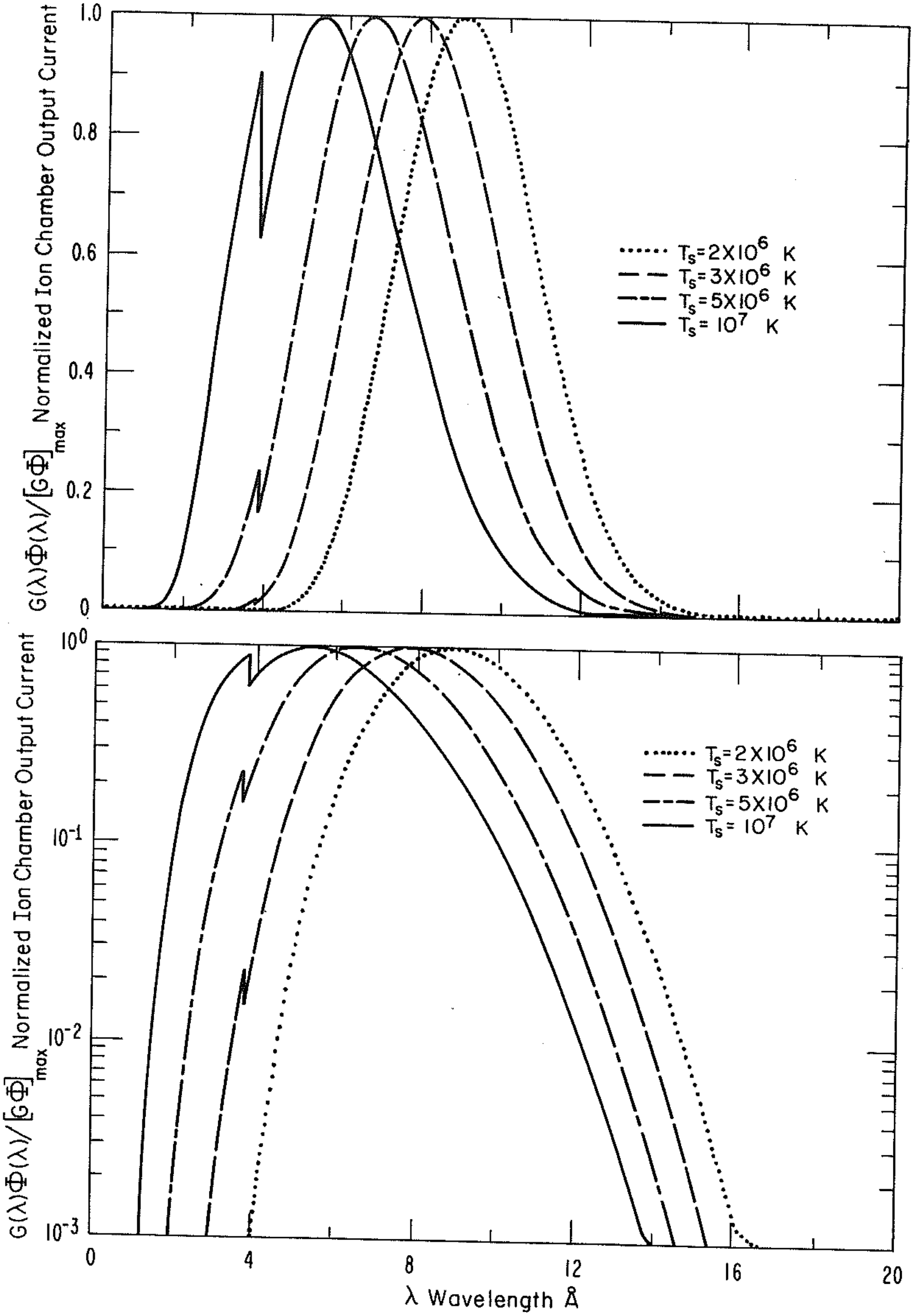

Figure 3.6. *The 1-8 A ion chamber response to isothermal free-free spectra.*

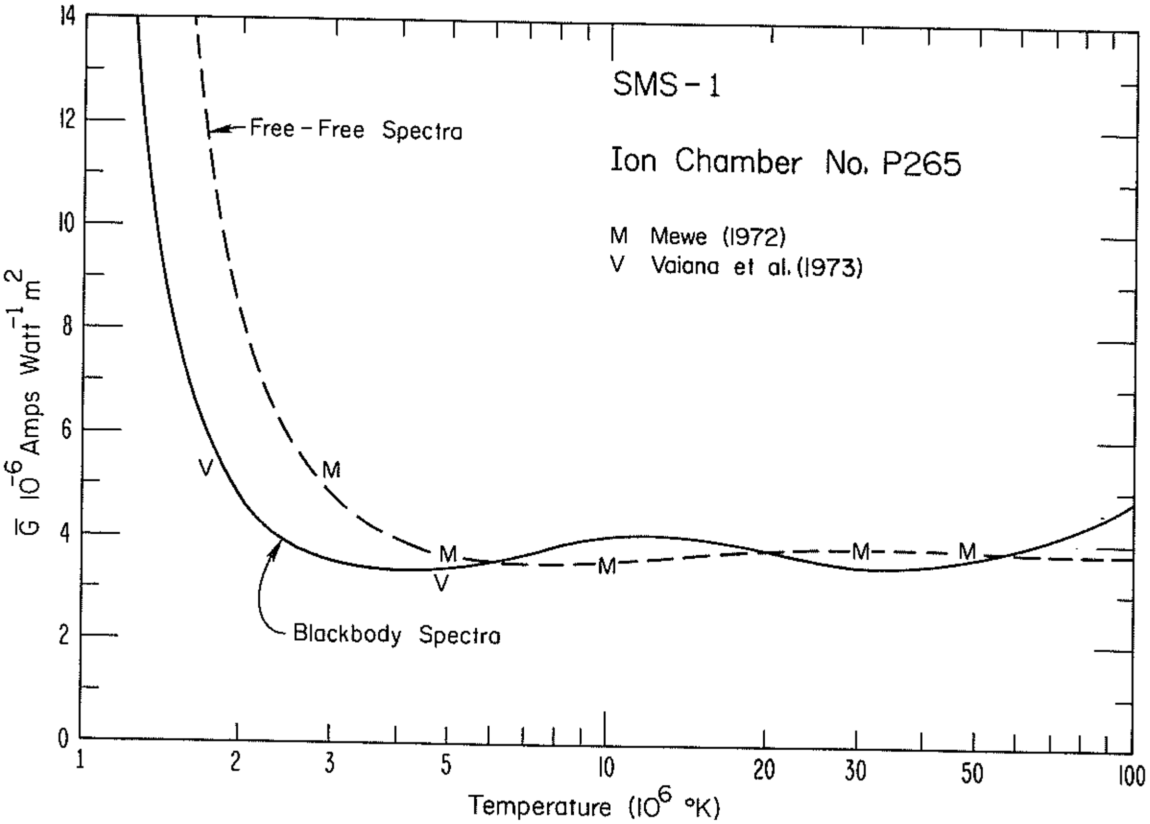

Figure 3.7. Calculated $\overline{G}$(1-8 A) as a function of source temperature T_S for isothermal theoretical spectra.

Figures 3.7 and 3.8 show $\overline{G}$ for the SMS-1 satellite for blackbody and free-free spectra as a function of source temperature. Note that $\overline{G}$ is fairly constant for blackbody spectra for source temperatures $T_s \geq 2x10^6$K, and for free-free spectra for $T_s \geq 3x10^6$K. A spectrum consisting of a sum of isothermal spectra will produce a similar $\overline{G}$ if the effective temperatures are all in the range where $\overline{G}$ is nearly constant. Therefore, one value of $\overline{G}$ may be satisfactory for high levels of solar activity when the 1-8 A flux is dominated by emission from source regions at temperatures $T_s \geq 3x10^6$K, but that value of $\overline{G}$ probably will not suffice for sunspot-minimum or very quiet Sun conditions because the quiet Sun includes significant X-ray emission from coronal regions at temperatures less than $3x10^6$K. Our knowledge of solar X-ray spectra has now improved to where we can do better than assume a blackbody spectrum, but it is interesting that the $\overline{G}$ values based on blackbody spectra are fairly close to those based on more current estimates of $\phi(\lambda)$. Theoretical studies of emission from

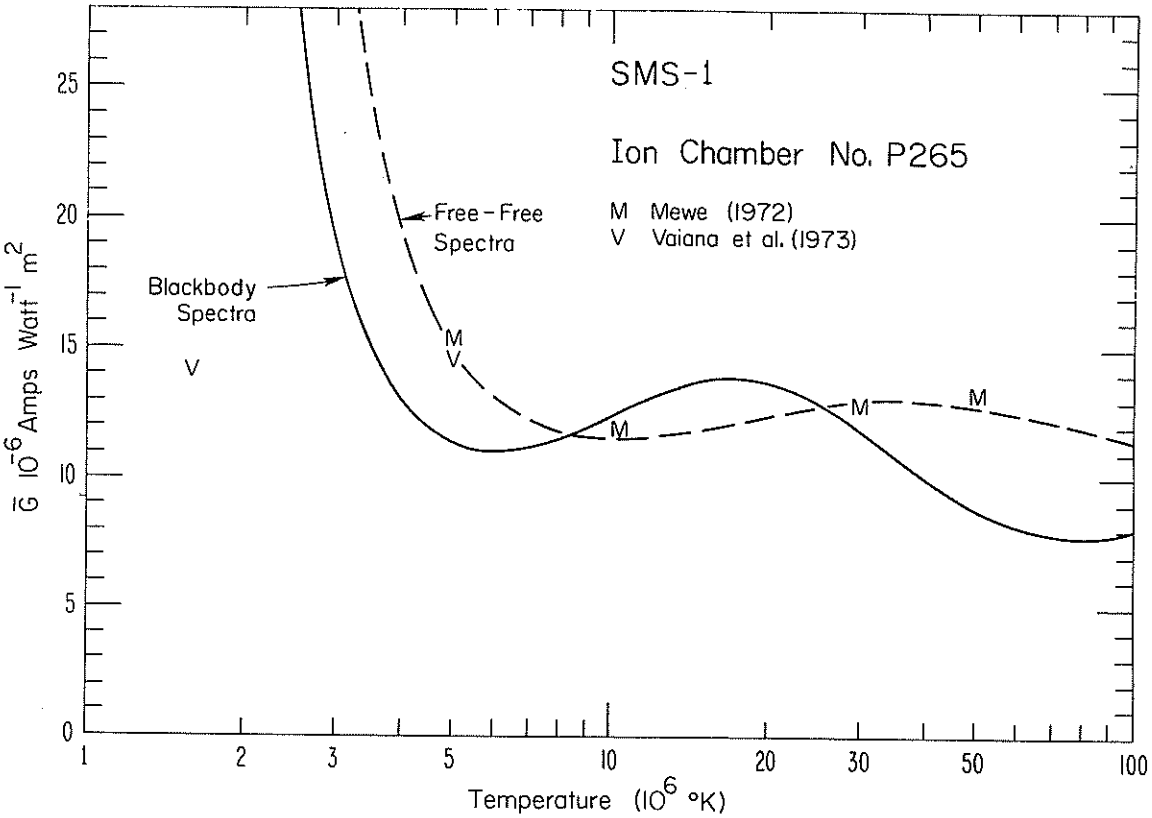

Figure 3.8. Calculated $\overline{G}(\frac{1}{2}$*-4 A) as a function of source temperature* T_S *for isothermal theoretical spectra.*

hot isothermal plasmas with the same composition as that of the solar atmosphere have provided improved estimates of solar spectra including line, recombination, and free-free thermal emission. $\overline{G}$ values based on the more complete theoretical spectra of Mewe (1972) and Vaiana et al. (1973) are also shown in Figures 3.7 and 3.8 as a function of source temperature, where the results agree well with the simple free-free results.

Wende (1971) developed the technique of computing $\overline{G}$ as a function of λ_1 and λ_2 for a set of solar spectra in order to optimize the λ_1 and λ_2 values so as to minimize the variations of $\overline{G}$ among the test spectra. Such calculations for SMS-1 for both blackbody and free-free spectra for source temperatures of 5, 7.5, 10, 25, 50, 75 and 100×10^6K indicated $\lambda_1 = 0.53$ A and $\lambda_2 = 4.1$ A for the short wavelength ion chamber, and $\lambda_1 = 0.9$ A and $\lambda_2 = 7.7$ A for the long wavelength ion chamber, which are fairly consistent with the $\frac{1}{2}$-4 A and 1-8 A bands used for the SMS/GOES solar X-ray monitoring measurements.

One difficulty with the calculations of $\overline{G}$ discussed above is that the solar spectrum certainly is not isothermal but involves a distribution of source regions as a function of temperature. Though spectra of solar flares include unusual emission lines that suggest portions of flares reach temperatures in the 10-30 x 10^6K range, solar spectra observations exhibit a general decrease in flux with decreasing wavelength below 10 A, except for emission lines and minor recombination edges (Neupert, 1971; Doscheck, 1972). Neupert et al. (1973) have observed spectra of solar flares that appear to include a peak with respect to wavelength near 12 A, but several problems complicate this conclusion, e.g., spectrometers that slowly scan in wavelength convolve the time dependence of a solar flare with its wavelength dependence. In conclusion, the increase in energy flux with decreasing wavelength at the long wavelength side of the 1-8 A passband for isothermal spectra with $T \geq 5 \times 10^6$K is unrealistic.

A second problem with the above calculations of $\overline{G}$ is that the set of theoretical spectra used are not weighted according to their relevance to the solar spectra when the soft X-ray flux is terrestrially important. Kreplin et al. (1962) showed that D-region SID's occur when the 1-8 A flux exceeds about 2×10^{-6}W m^{-2}. Smaller X-ray fluxes presumably generate ionization production rates smaller than that produced by cosmic rays in the lower D region or that produced by H Lyman α in the upper D region. Therefore, from a terrestrial viewpoint, solar spectra during fairly high levels of solar activity and during solar flares are important.

Culhane et al. (1969) and Pounds (1970) measured the solar spectra with low wavelength resolution (∿1/3 A below 4 A) during solar flares and high levels of solar activity. Figure 3.9 shows some of the spectra, and figures 3.10 and 3.11 illustrate the corresponding ion chamber responses. Figure 3.12 shows similar spectra of another solar flare, and figures 3.13 and 3.14 show the ion-chamber response. Note that the variations in spectra and ion-chamber response are smaller in figures 3.9-3.14 than in figures 3.2-3.6. Table 3.2 presents SMS-1 $\overline{G}$ values computed with $\phi(\lambda)$ based on their spectra. The standard deviation of $\overline{G}$ is only about 5% of the mean for $\frac{1}{2}$-4 A and 7% for 1-8 A for solar flare spectra. Using these results, the average $\overline{G}$ values in Table 3.3

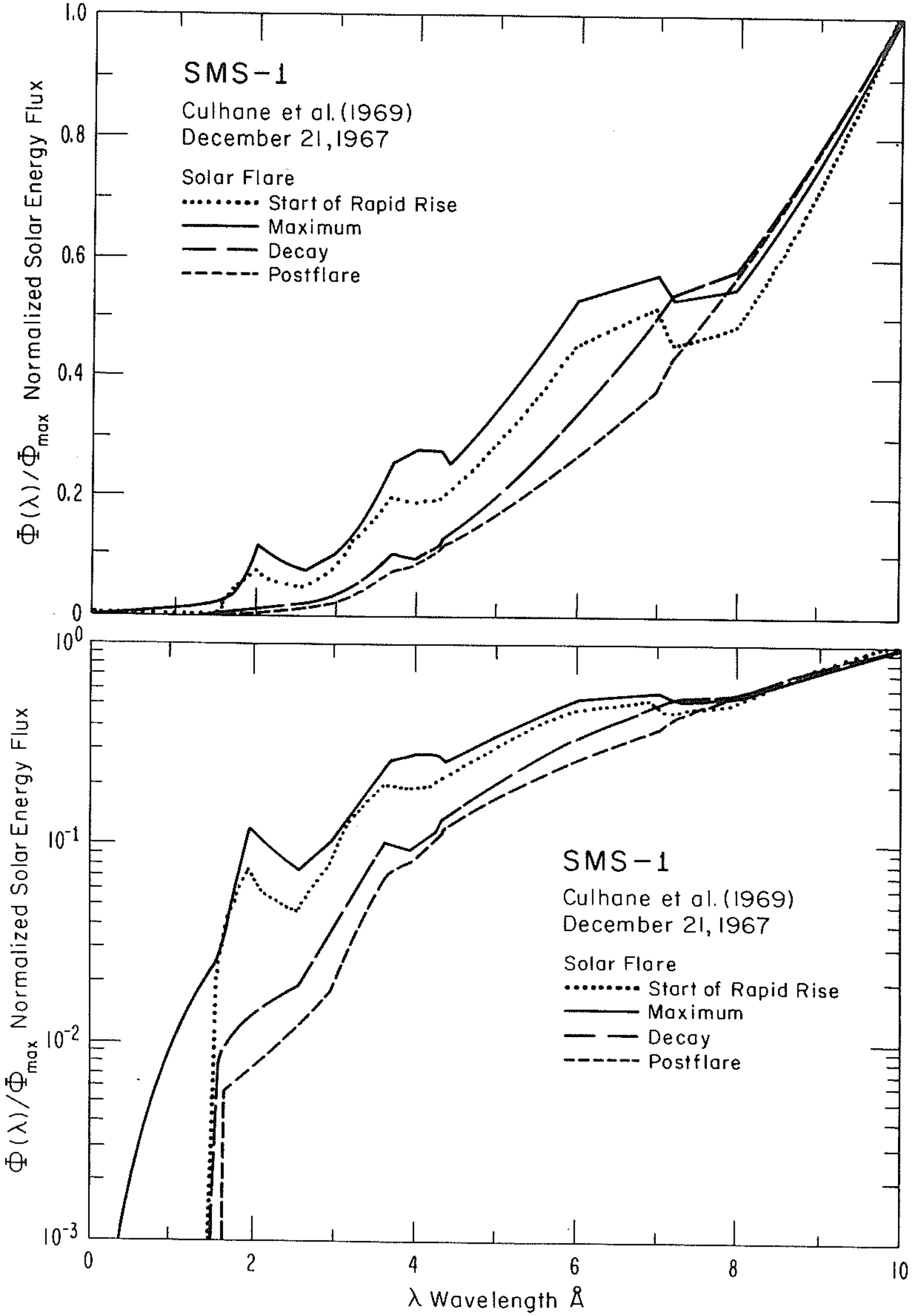

Figure 3.9. Solar flare spectra.

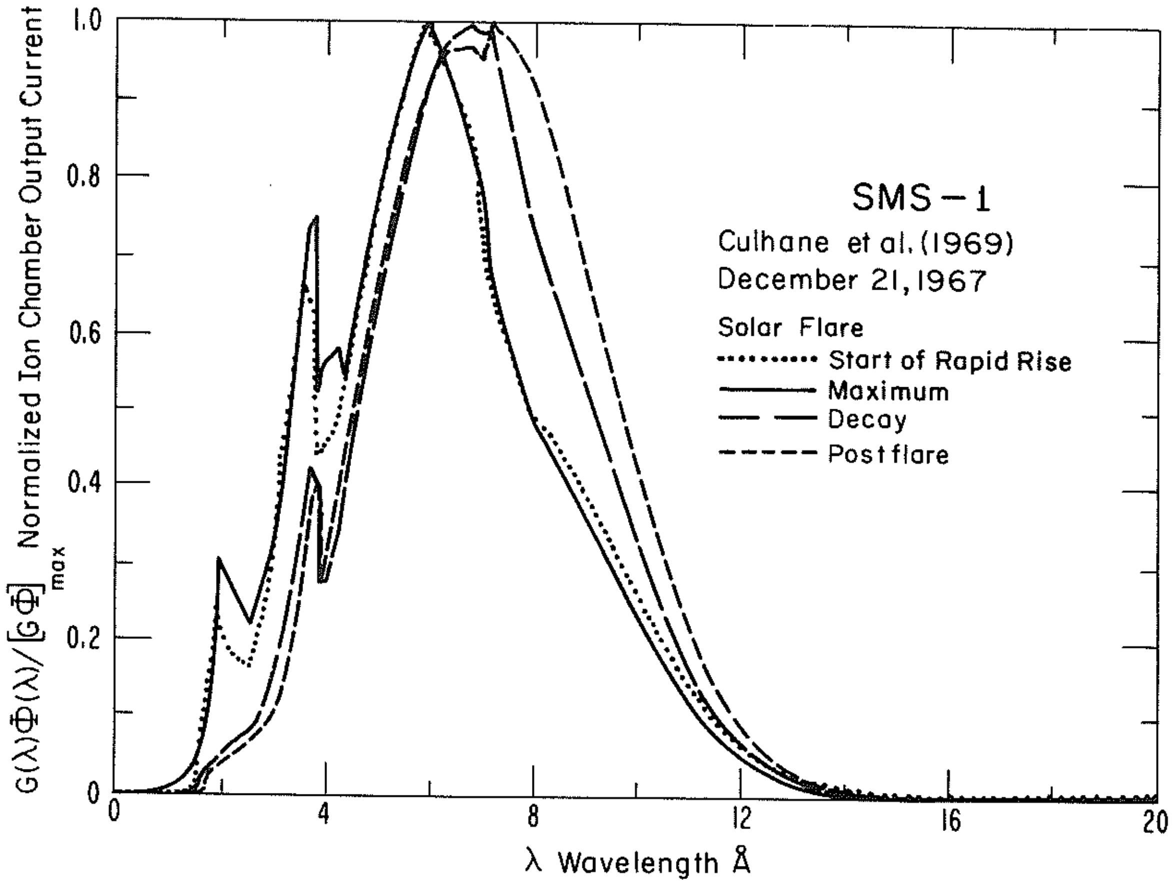

Figure 3.10. The 1-8 A ion chamber response to flare spectra.

were derived for SMS-1. The $\overline{G}$ values for SMS-2 in Table 3.3 were based on the SMS-1 results in Table 3.2 and figures 3.7 and 3.8, and on G_{SMS-2}/G_{SMS-1}. The GOES-1 results are based on an analysis like that for SMS-1 including the effect of a second thin filter window added to the GOES-1 instrument to block the solar ultraviolet light to prevent photoelectron ejection from the main X-ray filter window. These $\overline{G}$ values are now used in routine interpretation of the data and in the results discussed in the rest of this report. These average $\overline{G}$ values were picked to minimize the probable errors that can occur because of spectra variations when the solar X-ray flux is large enough to be terrestrially important. The differences in Table 3.3 from one satellite to another are caused by small differences in their window filters and because only the SMS-1 values included a revision of the theoretical results to provide a good fit to its calibration measurements, which lowered $\overline{G}(\frac{1}{2}$-4 A) by 3% and $\overline{G}$(1-8 A) by 19%.

Table 3.2. $\bar{G}(\frac{1}{2}\text{-}4\ \text{A})$ *and* $\bar{G}(1\text{-}8\ \text{A})$ *for SMS-1 for Solar Flare Spectra*

Date	Flare Condition	Universal Time	$\bar{G}(\frac{1}{2}\text{-}4\ \text{A})$	$\bar{G}(1\text{-}8\ \text{A})$
Oct. 26, 1967	Preflare	06:03:30	$1.21\text{x}10^{-5}$	$4.21\text{x}10^{-6}$
	Early Flash Phase	06:10:00	$1.23\text{x}10^{-5}$	$3.99\text{x}10^{-6}$
	Late Flash Phase	06:11:30	$1.22\text{x}10^{-5}$	$3.80\text{x}10^{-6}$
	Early Maximum	06:13:45	$1.19\text{x}10^{-5}$	$3.76\text{x}10^{-6}$
	Late Maximum	06:16:00	$1.19\text{x}10^{-5}$	$3.91\text{x}10^{-6}$
	Early Decay	06:20:00	$1.14\text{x}10^{-5}$	$4.03\text{x}10^{-6}$
	Mid Decay	06:23:45	$1.10\text{x}10^{-5}$	$4.02\text{x}10^{-6}$
	Late Decay	06:28:45	$1.17\text{x}10^{-5}$	$3.92\text{x}10^{-6}$
Dec. 21, 1967	Early Rapid Rise	01:54:10	$1.29\text{x}10^{-5}$	$4.07\text{x}10^{-6}$
	Maximum	01:54:45	$1.22\text{x}10^{-5}$	$3.86\text{x}10^{-6}$
	Decay	01:55:57	$1.21\text{x}10^{-5}$	$3.89\text{x}10^{-6}$
	Post Flare	01:59:00	$1.22\text{x}10^{-5}$	$3.80\text{x}10^{-6}$
April 27, 1962	Preflare	2109-2117	$1.22\text{x}10^{-5}$	$5.95\text{x}10^{-6}$
	Early Rise	2301-2304	$1.26\text{x}10^{-5}$	$4.52\text{x}10^{-6}$
	Late Rise	2304-2307	---------	$3.77\text{x}10^{-6}$
May 3, 1962	Early Rise	0648	$1.32\text{x}10^{-5}$	$4.90\text{x}10^{-6}$
	Mid Rise	0652	$1.23\text{x}10^{-5}$	$3.91\text{x}10^{-6}$
	Maximum	0655	$1.23\text{x}10^{-5}$	$3.89\text{x}10^{-6}$
	Quiet Sun	1145	$2.89\text{x}10^{-5}$	$1.07\text{x}10^{-5}$
	Average, excluding quiet sun =		$1.22\text{x}10^{-5}$	$4.12\text{x}10^{-6}$
	Standard Deviation =		$0.05\text{x}10^{-5}$	$0.52\text{x}10^{-6}$
	Average, excluding preflare and postflare =		$1.21\text{x}10^{-5}$	$4.02\text{x}10^{-6}$
	Standard Deviation =		$0.06\text{x}10^{-5}$	$0.29\text{x}10^{-6}$

References for the solar flare spectra measurements, which have low wavelength resolution, are Culhane et al. (1964, 1969) and Pounds (1970). The $\frac{1}{2}$-4 A results for the 1962 flares are not very meaningful because those spectra measurments were good only at wavelength longer than 5 A.

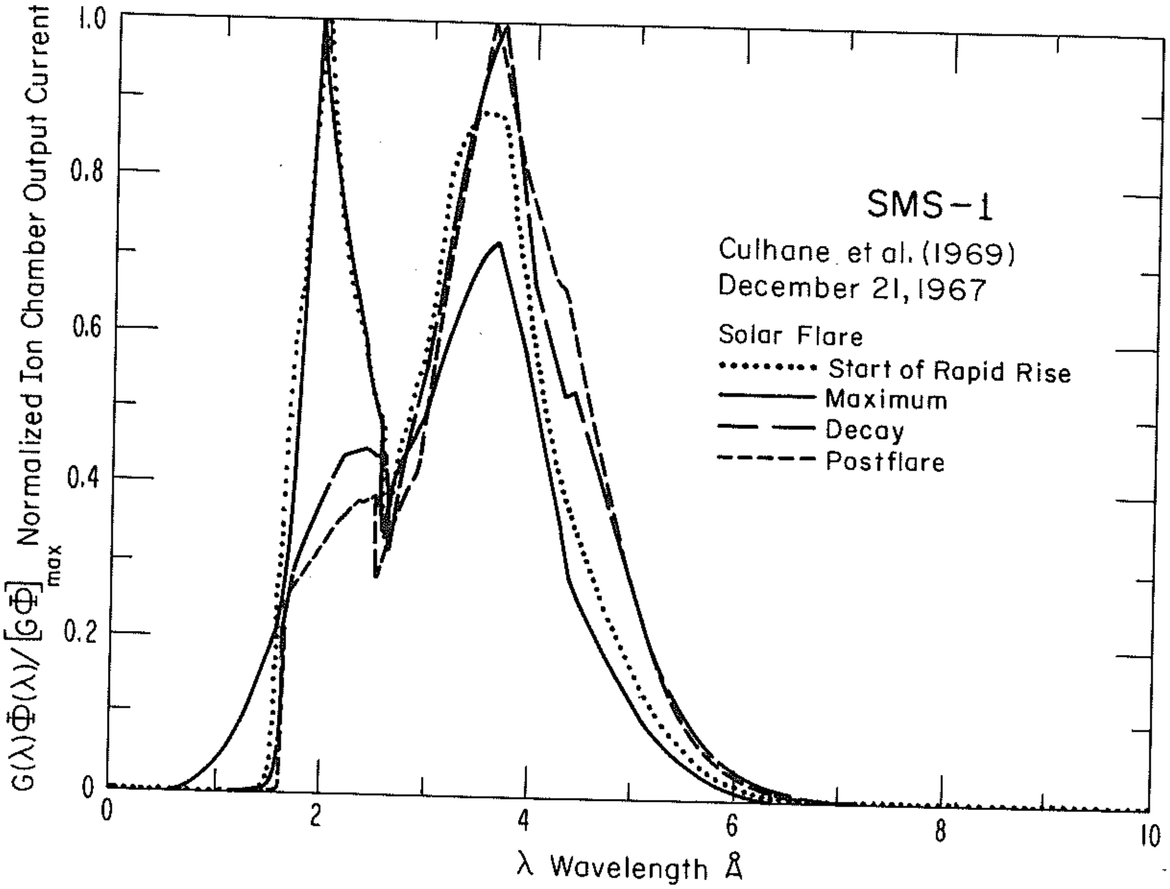

Figure 3.11. The $\frac{1}{2}$-4 A ion chamber response to flare spectra.

Table 3.3 $\overline{G}$ Adopted for SMS-1, SMS-2, and GOES-1

Standard Transfer Functions for Archival Data

Satellite	$\overline{G}(\frac{1}{2}$-4 A)	$\overline{G}$(1-8 A)
SMS-1	1.23×10^{-5}	4.00×10^{-6}
SMS-2	1.28×10^{-5}	4.96×10^{-6}
GOES-1	1.27×10^{-5}	4.09×10^{-6}

amps W^{-1} m^2

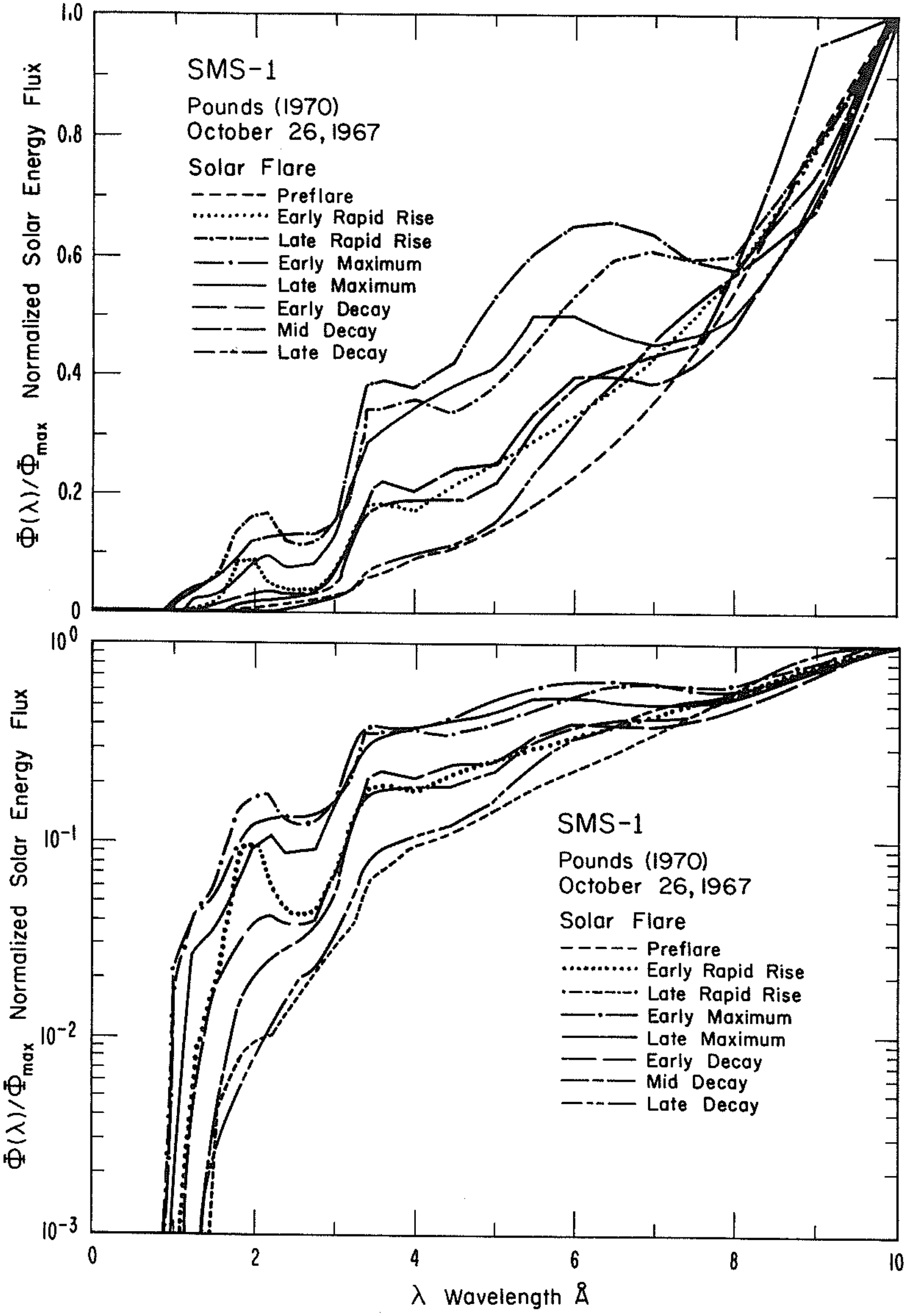

Figure 3.12. Solar Flare spectra.

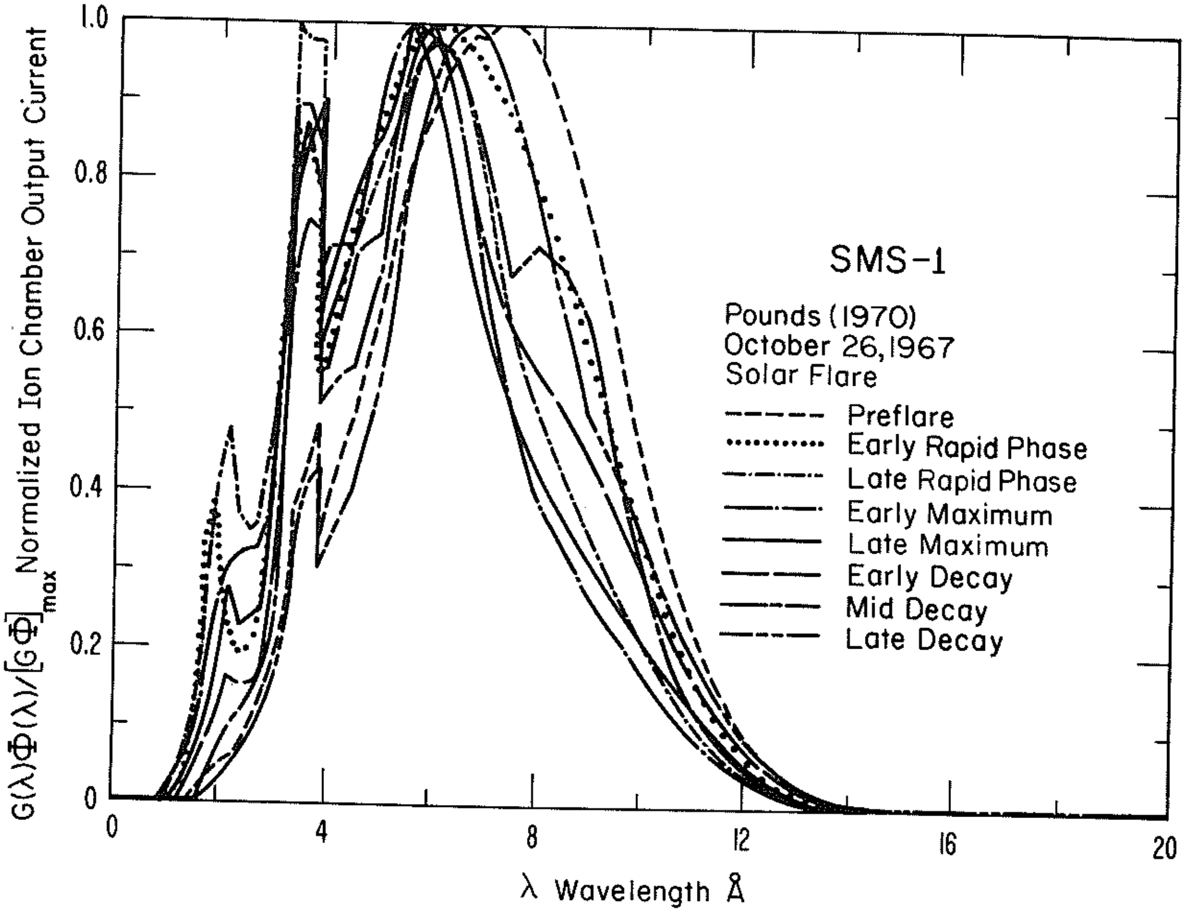

Figure 3.13. The 1-8 A ion chamber response to flare spectra.

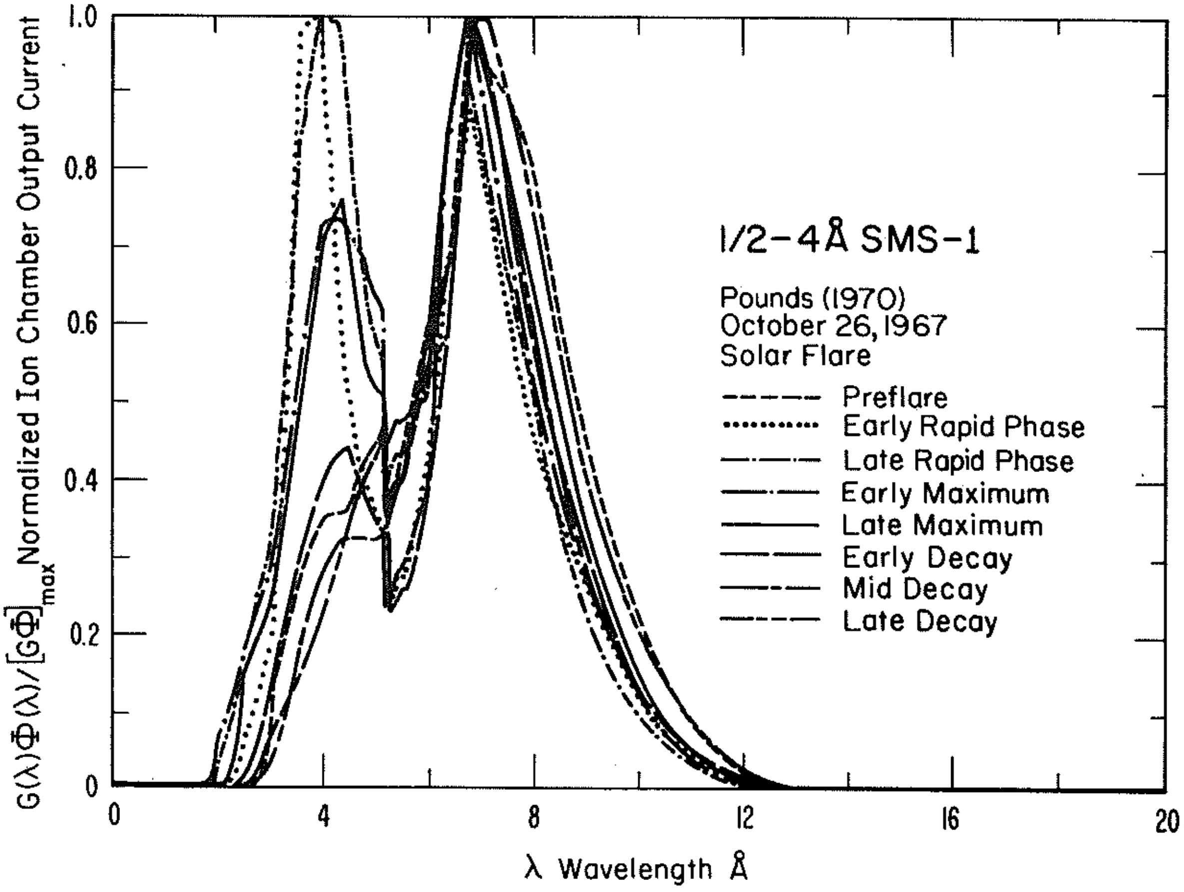

Figure 3.14. The $\frac{1}{2}$-4 A ion-chamber response to flare spectra.

3.3 Solar Spectrum Corrections for Low Flux Levels

As the solar flux decreases from the levels of terrestrial importance to the very low quiet-Sun levels of sunspot minimum years, the solar X-ray spectrum becomes too soft to be consistent with the values derived with the standard transfer functions of Table 3.3, where the $\frac{1}{2}$-4 A flux measurements will be the first to be significantly affected. Corrections to the archive data can then be made by developing a model for the solar X-ray spectra and calculating the corresponding $\overline{G}_r$ for the particular low flux conditions of interest. Then the revised flux Φ_r can be determined from the archive data flux Φ_A and the standard transfer functions $\overline{G}_S$ in Table 3.3 from $\Phi_r = \Phi_A \overline{G}_S/\overline{G}_r$. Isothermal free-free spectra for quiet coronal temperatures $T \sim 2 \times 10^6$K are one example of spectrum assumptions that have been used in the past. For free-free or blackbody spectrum assumptions figures 3.7 and 3.8 can be used to determine $\overline{G}_r$ for an assumed source temperature. Considering the steepness of $\overline{G}(T_S)$ for $T_S < 3 \times 10^6$K, it is clear that for very low flux intensities or quiet Sun conditions, $\Phi(\frac{1}{2}$-4 A) values are rather meaningless and unsuitable for spectrum corrections. However, the time variations in the $\frac{1}{2}$-4 A flux measurements are still useful for low flux levels for indicating time variations in solar activity.

3.4 X-Ray Flux Ratio $\Phi(\frac{1}{2}$-4 A)/Φ(1-8 A).

The ratio of flux in the two wavelength channels can be used to check whether the flux measurements are consistent with the use of the standard transfer functions. For the spectra discussed in section 3.2, the solar flux measured by the ion chamber was calculated in two ways: (1) the expected flux measurement Φ_A was calculated like all archive data using the standard transfer functions and then using the ion-chamber output current produced by the particular spectrum involved, and (2) the incident flux Φ_I was calculated directly from the theoretical or model spectra. The flux ratios, $\Phi_A(\frac{1}{2}$-4 A)/Φ_A(1-8 A) and $\Phi_I(\frac{1}{2}$-4 A)/Φ_I(1-8 A) were then compared. Figure 3.15 shows the percent error in the flux ratio that would occur in the archive data if the solar spectra were isothermal or like those of Culhane et al. (1969) or Pounds (1970),

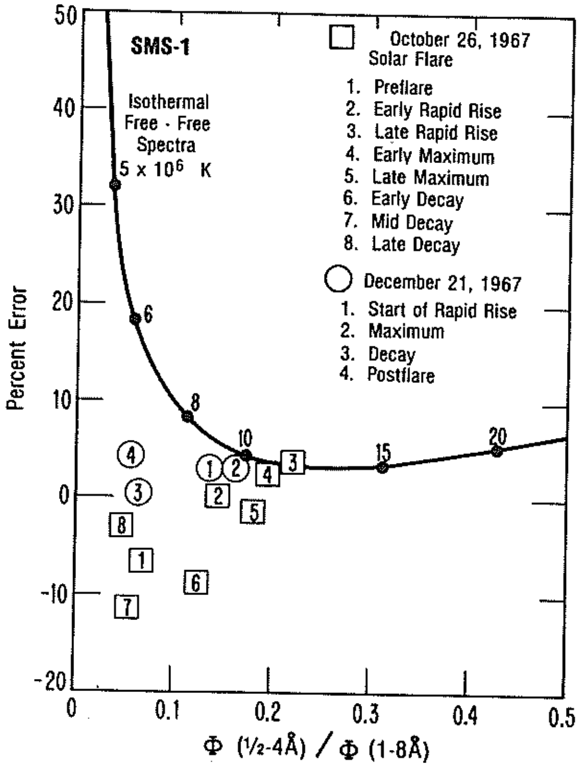

Figure 3.15. Percent error in X-ray flux based on the standard transfer functions for several particular X-ray spectra. The solar flare spectra are based on Culhane et al. (1969) and Pounds (1970).

i.e.,

Percent Error =

$$\left[\frac{\Phi_A(\frac{1}{2}\text{-4 A})/\Phi_A(\text{1-8 A})}{\Phi_I(\frac{1}{2}\text{-4 A})/\Phi_I(\text{1-8 A})} - 1\right] 100\%. \qquad (3.4)$$

If the measured flux ratio exceeds 0.1, spectral variations probably cause errors in the ratio of archival flux data of less than 10%. If the observed ratio is about 0.05, errors in using the standard transfer functions may be as large as 20%. As the observed ratio decreases and the estimated error in the ratio of archival flux values increases, most of the error involved is in the $\frac{1}{2}$-4 A flux measurement. In other words, as solar spectra evolve from the hot spectra of flares and high levels of solar activity toward quiet Sun or sunspot minimum conditions, the standard assumption will fail sooner for $\frac{1}{2}$-4 A than for 1-8 A.

Figure 3.16 shows the observed flux ratio for several time sequences starting at quiet preflare conditions and ranging through the rapid rise, peak, and decay of solar flares. These SMS-1 measurements were corrected for the photoelectron effect discussed in 4.5. The standard $\overline{G}$ assumption is believed to be quite adequate for $\Phi(\text{1-8 A}) \geq 10^{-6}\text{W m}^{-2}$ and for $\Phi(\frac{1}{2}\text{-4 A})$ for flux levels of terrestrial importance. However, Figure 3.16 indicates the standard assumption fails for $\Phi(\frac{1}{2}\text{-4 A}) \lesssim 10^{-7}\text{W m}^{-2}$, particularly during the late decay of solar flares.

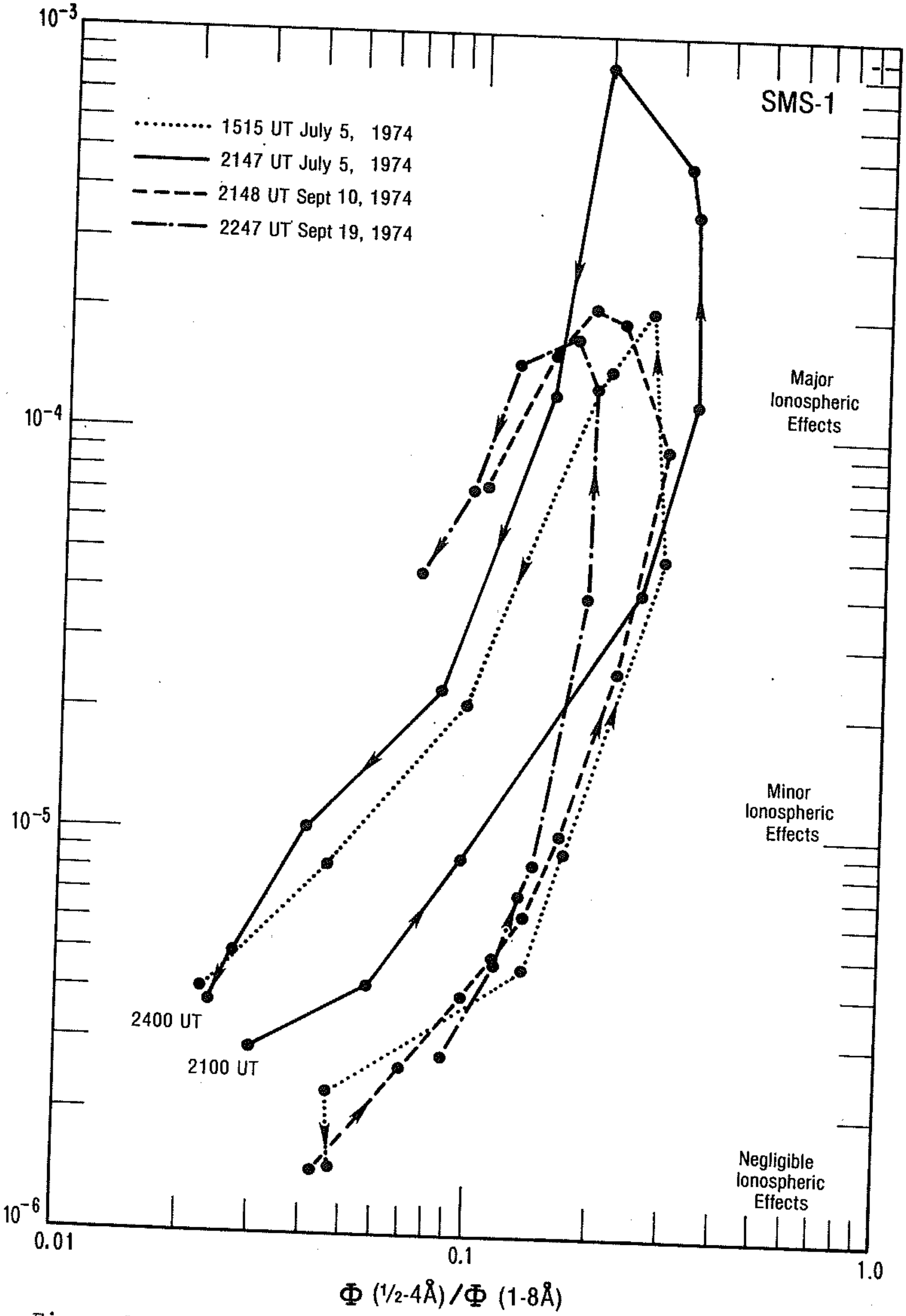

Figure 3.16. Observed solar X-ray flux ratios for X-ray intensities of terrestrial significance.

4. COMPLICATIONS IMPORTANT TO DATA INTERPRETATION

4.1 Range Switching Transients

Each X-ray channel achieves both a large dynamic range and high intensity resolution through covering the intensity range by four sequential ranges, where adjacent ranges slightly overlap. The four ranges of gain in the satellite electronics are obtained by two switches, one in the two-range electrometer preamplifier, which changes its gain by a factor of 100, and the second in a two-range attenuator, which changes the gain by a factor of 10. The attenuator switch changes position during each change in range whereas the switch in the electrometer preamplifier acts only during the change from the second to third gain ranges. Each switch in gain causes a transient spike in the data as shown in figure 4.1. When the X-ray flux increases with time, the spikes exceed the true X-ray flux. When the X-ray flux decreases, the spikes are downward. Each spike consists of a step jump, followed by an exponential decay with a time constant τ usually about 3.5 to 5.5 sec., depending on the channel and range involved. The size of the observed jump is typically 3.5 to 12 times the pre-jump level. It varies from one case to another because the time of its occurrence varies with respect to the 3 sec data sample period. About five data points (15 sec) after a switch are affected by the transient response in the electronics. Corrections can be made by estimating the error by

$$\underset{\text{estimate}}{\Phi(t)} = \underset{\text{observed}}{\Phi(t)} - \underset{\text{error}}{\Phi(t)} , \tag{4.1}$$

where

$$\Phi_{\text{error}} = \Delta\Phi_{\substack{\text{observed}\\ \text{jump}}}\, e^{-(t-t_{\text{jump}})/\tau} , \tag{4.2}$$

t_{jump} is the time at the observed peak of the spike, and

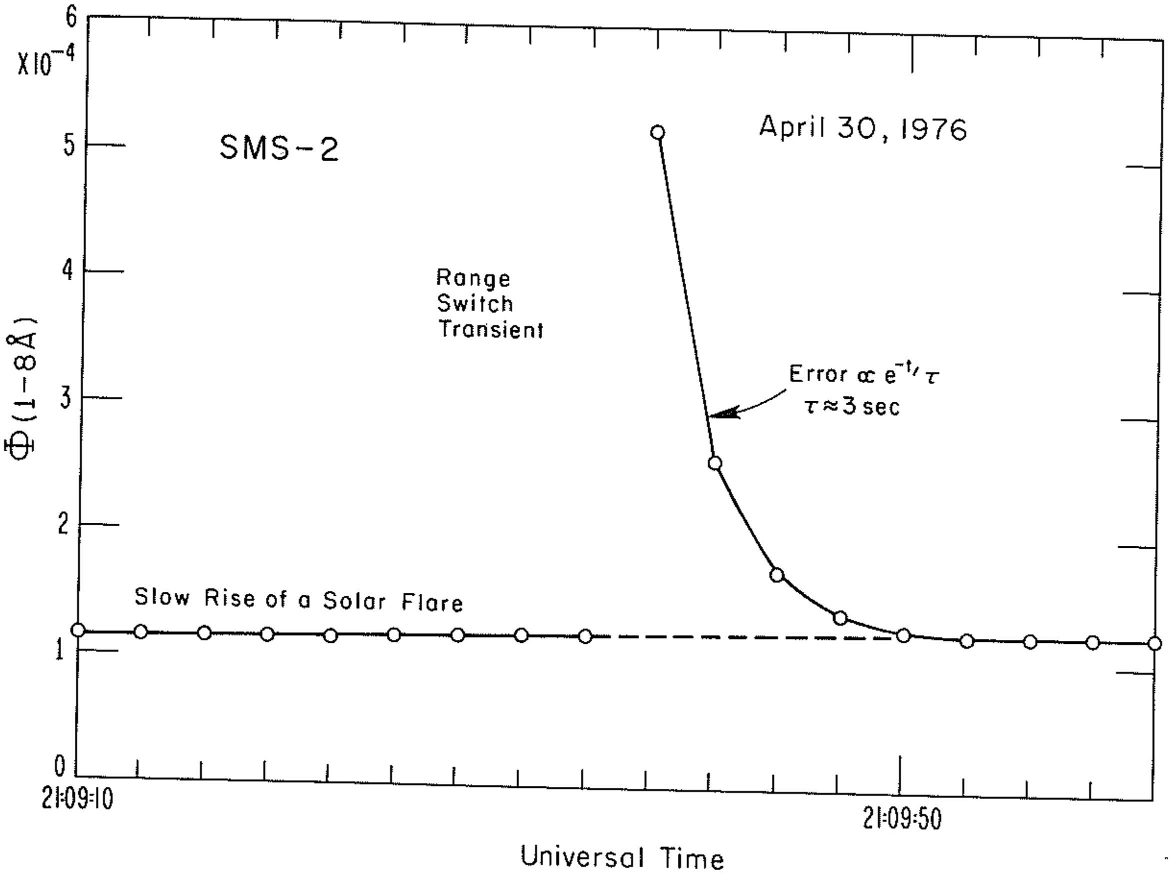

Figure 4.1. Example of the transient response in X-ray measurements that occurs when the gain range automatically switches to the next lower gain range, i.e., the next higher X-ray flux range.

$$\Delta\Phi_{\text{jump}} = \Phi\,(t_{\text{jump}})_{\text{observed}} - 2\Phi\,(t_{\text{jump}} - 3\text{ sec})_{\text{observed}} + \Phi(t_{\text{jump}} - 6\text{ sec})_{\text{observed}} \quad ,(4.3)$$

which uses a linear extrapolation of the pre-jump trend. The first datum after a switch in gain is flagged in the archive data with the expectation that in most applications the only need is to mark the resultant spike in the data as an instrumental effect and not a real spike in solar flux. Note that at least four more 3-sec samples after the flagged datum are affected by the switching transient but are not flagged.

4.2 Intensity Resolution

Because of the high intensity resolution and moderate time resolution, the SMS/GOES solar X-ray data are being used to study the time rate of change of X-ray flux during solar flares. The intensity resolution is about 0.2% to 0.3% of the maximum flux of the particular gain range involved. Consequently, the smallest measurable change in X-ray flux in one 3-sec period varies by a factor of ten from one gain range to the next. This must be taken into consideration in studies of $d\Phi/dt$.

4.3 Instrument Temperature

The temperature of the electronics and temperature of the ion-chamber telescope are monitored in order to provide corrections to the X-ray data if the temperatures deviate significantly from the planned operating temperature. The corrections vary over each intensity range and from one range to another, but the maximum correction in a range is typically less than 0.1% per °C of difference in temperature with respect to the design temperature (∿24°C). Operating temperatures for the X-ray instruments are stable over most days but drift slowly from a maximum in winter of about 23° - 24°C to a minimum near summer solstice of about 18°. Corrections for these temperature variations are negligible.

The main deviations from these average operating temperatures occur during eclipses of the Sun. Figure 4.2 shows that during totality, the temperature of the X-ray instrument decreases approximately linearly with time at the rate of about 0.23°C/min. The longer the duration of the eclipse, the greater the drop in temperature. Partial eclipse and changes in satellite operation cause small changes before and after totality. The temperature then exponentially rises, asymptotically approaching the normal operating temperature with a decay time constant of about 4 hr. The X-ray data available from the archive data tapes have no corrections for these small shifts in operating temperature. The estimates of error should therefore increase slightly after an eclipse with a time function like that in figure 4.2, and a maximum error estimated to be less than 3%.

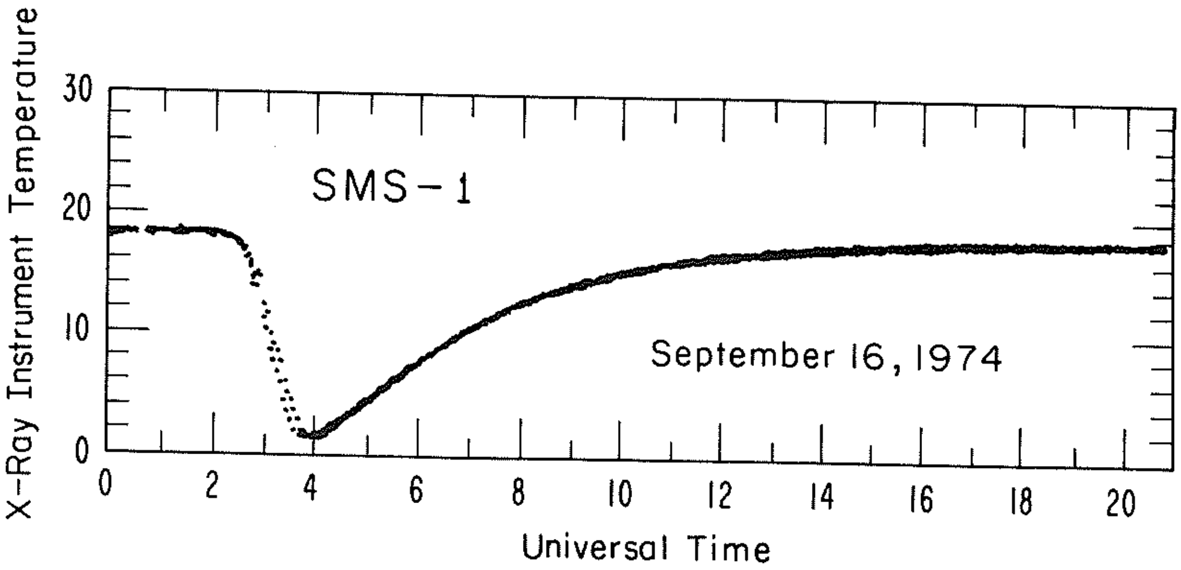

Figure 4.2. Temperature response to an eclipse of the Sun by the Earth at the SMS-1 satellite. Two curves of temperature are shown, one for the temperature of the X-ray electronics and one for the X-ray telescope temperature. The two temperatures are nearly equal so the two curves are superimposed.

4.4 Saturation

The flare of 2144 UT July 5, 1974, was large enough to drive the SMS-1 $\frac{1}{2}$-4 A channel into saturation at 1.7 x 10^{-4}W m^{-2}. The 1-8 A channel measured a peak flux of 1.13 x 10^{-3}W m^{-2}, without clear signs of saturation, although this flux is approximately the expected maximum measurable 1-8 A flux.

4.5 Photoelectron Bias in SMS-1

The solar ultraviolet flux shining on the X-ray ion chambers induces photoelectron ejection which generates a current that is weakly coupled into the ion chamber current measurements on SMS-1, causing negative telemetry signals when the solar X-ray flux is very low. This problem was eliminated on SMS-2 and GOES-1 by revising the circuits to reduce the coupling of the photoelectron current. A thin absorption window was also added to the GOES-1 X-ray telescope to block the UV radiation.

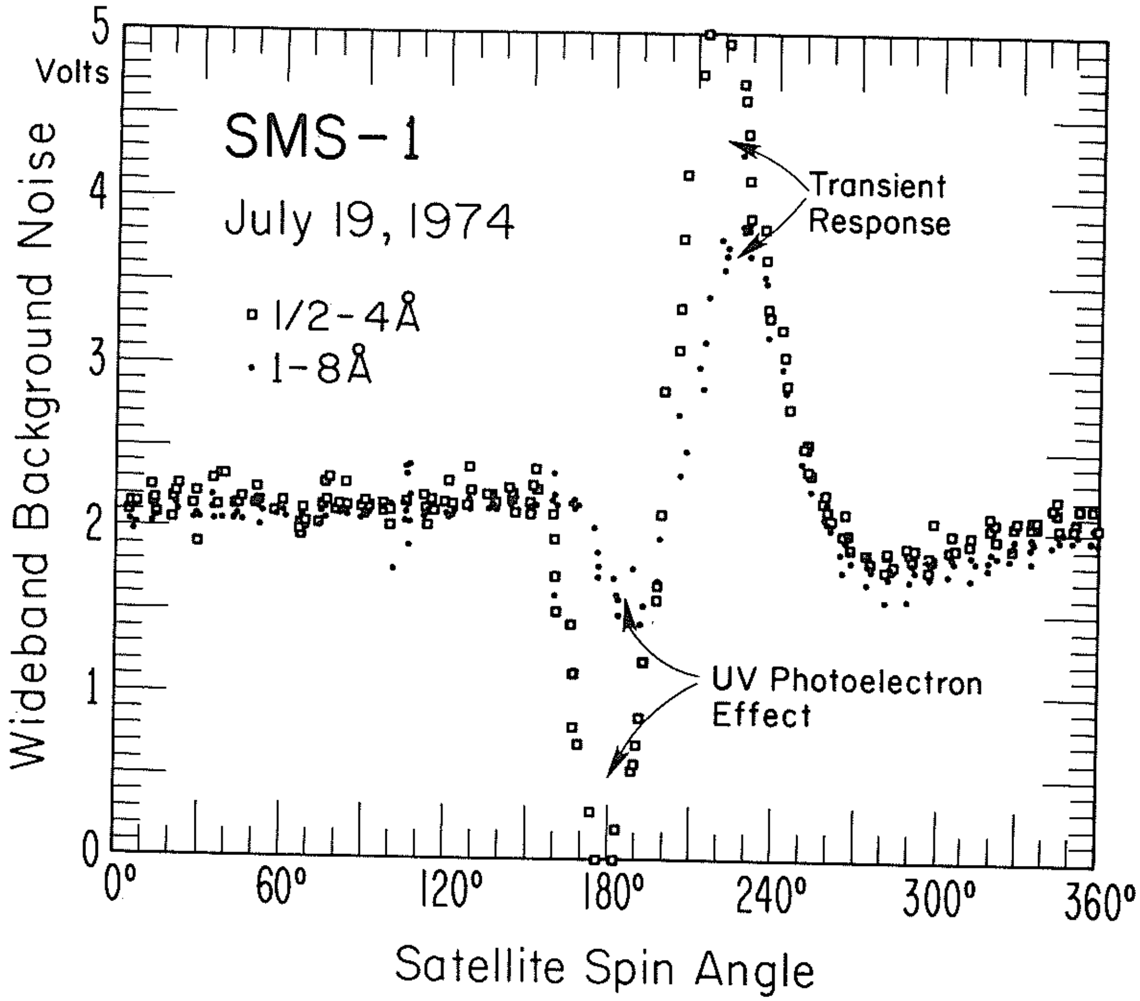

Figure 4.3. Evidence for photoelectron effect in SMS-1. Data provided by Mr. Harry Farthing, NASA GSFC.

Figure 4.3 shows observations of the wideband background channel that monitors the electrometer amplifier output for SMS-1, where a negative transient followed by a positive one is induced in the measurements by the solar UV radiation as the X-ray detector scanned across the Sun. The normal response from X-rays dominates over the UV response for $\Phi(1\text{-}8\ A) \geq 10^{-6}W\ m^{-2}$ and $\Phi(\frac{1}{2}\text{-}4\ A) \geq 10^{-7}W\ m^{-2}$, but at lower X-ray flux levels large relative errors occur in the SMS-1 measurements because of this photoelectric effect. Large flux values, where the photoelectric effect in SMS-1 is negligible, were used to determine the relationship between SMS-1 and SMS-2 flux measurements (see sect. 5). This relationship was then used together with SMS-2 measurements for low flux values to estimate what the SMS-1 measurements would be if there were no photoelectric effect. These estimates were then compared with the concurrent SMS-1 measurements to determine an approximate correction for removing the error in the SMS-1 data caused by the photoelectric effect. The results are as follows:

$$\Phi(1\text{-}8\ \text{A})_{\text{corrected SMS-1}} = \Phi(1\text{-}8\ \text{A})_{\text{measured SMS-1}} + 1.7 \times 10^{-7}\ (\text{W m}^{-2}) \tag{4.4}$$

and

$$\Phi(\tfrac{1}{2}\text{-}4\ \text{A})_{\text{corrected SMS-1}} = \Phi(\tfrac{1}{2}\text{-}4\ \text{A})_{\text{measured SMS-1}} + 4.0 \times 10^{-8}\ (\text{W m}^{-2})\ . \tag{4.5}$$

The archive data give the measured values and do not include any corrections. Because of range limits in the SMS-1 X-ray electronics, the measured flux values do not go below $\Phi(1\text{-}8\ \text{A}) = -7.234 \times 10^{-8}$, or $\Phi(\frac{1}{2}\text{-}4\ \text{A}) = -8.342 \times 10^{-9}$ W m^{-2}. When the measured values are at these limits, the results from (4.4) or (4.5) are then estimates of an upper limit to the true solar X-ray flux. In other words, the SMS-1 results cannot be used to determine X-ray fluxes below 10^{-7} W m^{-2} for 1-8 A or 3.1×10^{-8} W m^{-2} for $\frac{1}{2}$-4 A. In summary, the photoelectric effect is a problem only for SMS-1 results for low solar flux intensities, lower than the intensities of terrestrial importance. Note that at those low flux intensities, corrections should also be made for the fact that the solar X-ray spectrum is probably inconsistent with the constant transfer function $\overline{G}$ used to determine Φ measured (see sect. 3.).

4.6 Missing Points

Whenever the received telemetry signal was noisy so that the ground-based data processing system was unable to synchronize with the data code to be able to pick out the X-ray data from among many other data sets, then no data were recorded for that 3-sec set. Usually the interval betweem archive data is three seconds, but occasionally one or several will be missing. The archive data tapes do not flag these cases since they are evident from the fact that the time between adjacent points increases to more than 3 seconds.

4.7 Isolated Bad Points

Telemetry noise and other noise occasionally cause an X-ray flux measurement to be highly erroneous. These cases are usually very evident because the flux values differ greatly with respect to adjacent values. Whenever a flux measurement $\Phi(t_i)$ differed by more than 20% with respect to the prior measurement $\Phi(t_{i-1})$ and by more than 20% in the same direction with respect to the next later measurement $\Phi(t_{i+1})$, $\Phi(t_i)$ was concluded to be noise and was replaced in the archive data tapes with a corrected single point value based on the average of adjacent points;

$$\Phi(t_i)_{\text{corrected}} = \frac{\Phi(t_{i-1}) + \Phi(t_{i+1})}{2} \quad . \qquad (4.6)$$

Whenever any of the three values were flagged for any other reason, this correction was not made. The test in (4.6) was performed separately for both the $\frac{1}{2}$-4 A data and 1-8 A data. Corrected single points are identified in the archive data magnetic tapes with a special flag (see sect. 7).

4.8 X-Ray Telescope Elevation Angle

Because the satellite spin axis was perpendicular to the equatorial plane, the angle between the X-ray telescope axis and the satellite spin axis was adjusted by increments of 1/4° so that the telescope would scan the Sun. The telescope angle is adjusted from day to day as needed to track the Sun as its declination varies over the year from summer to winter solstice. The telescope angle was measured and provided in the telemetry data. These measurements showed the telescopes were daily set at the positions expected to be best for scanning the Sun. During the early check out of the satellite and its experiments in the first several weeks after launch, the X-ray telescope was stepped in angle to scan the Sun along the direction of the satellite spin axis. Unfortunately, these tests were made at times when the X-ray flux was extremely low so they did not provide a precise measure of the X-ray instrument response as a function of telescope elevation angle. Figure 4.4 shows the 1-8 A X-ray output versus elevation angle for GOES-1 taken over about a half-

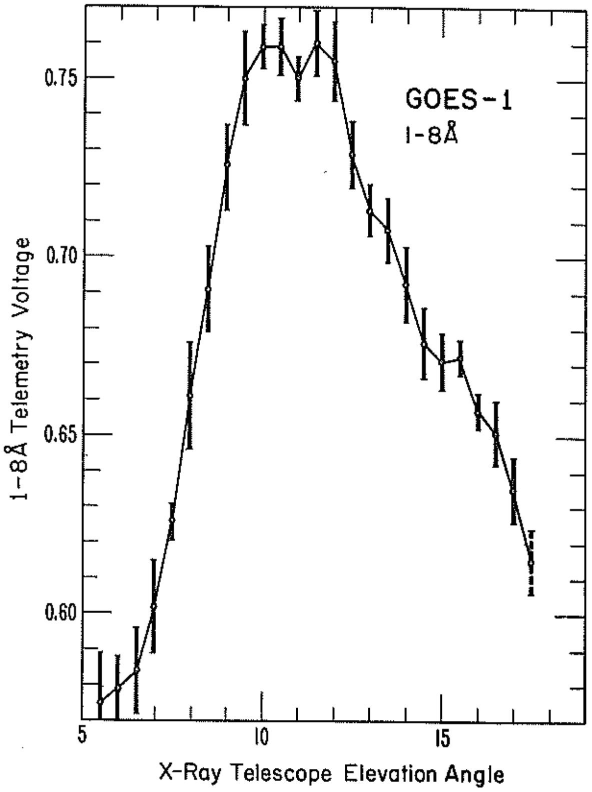

Figure 4.4. Observed elevation angle dependence.

hour period on October 19, 1975, when the solar declination was about 10° south. The error bars are based on the rms deviation of the measurements accumulated for each telescope angle. The collimator causes the steep sides of the response. The small angle side of the response is steeper than the large angle side because of the shape of the collimator. The detailed shape of the elevation angle response also depends on the distribution of X-ray source regions on the Sun. According to the Lockheed OSO-8 data in <u>Solar Geophysical Data</u>, the main solar X-ray sources were in the elevation angle range 8' North to 10' South of the center of the solar disk on October 19, 1975.

Figure 4.5 shows the theoretical elevation angle response for the 1-8 A ion chamber for a point X-ray source. The angle between the telescope axis and the satellite-Sun line equals the telescope elevation angle, measured positive to the south, plus the solar declination, measured positive to the north. The solid line is appropriate for long wavelengths ($\lambda > 8$ A), where the ion chamber response depends on the portion of the filter window that is illuminated. The dashed line is for short wavelengths ($\lambda < 1$ A) where the ion chamber output is proportional to the illuminated volume of the ion chamber. The mid wavelength response should fall between these two curves. Because solar spectra are strong on the long wavelength side of the detector and weak on the short wavelength side, the elevation angle response for solar X-rays should be closer to the solid curve than to the dashed curve. When the telescope elevation angle is too small, it points north of the Sun where the outside telescope wall occults the Sun. When the telescope points south of the Sun, the collimator fins located in front of the $\frac{1}{2}$-4 A ion chamber occult the Sun viewed at the

1-8 A ion chamber. No collimator fins are directly in front of the 1-8 A ion chamber. Note the similarity between figures 4.4 and 4.5. The 1-8 A measurements should be less in error than being 2% too low for errors less than one degree in pointing the telescope at the sun.

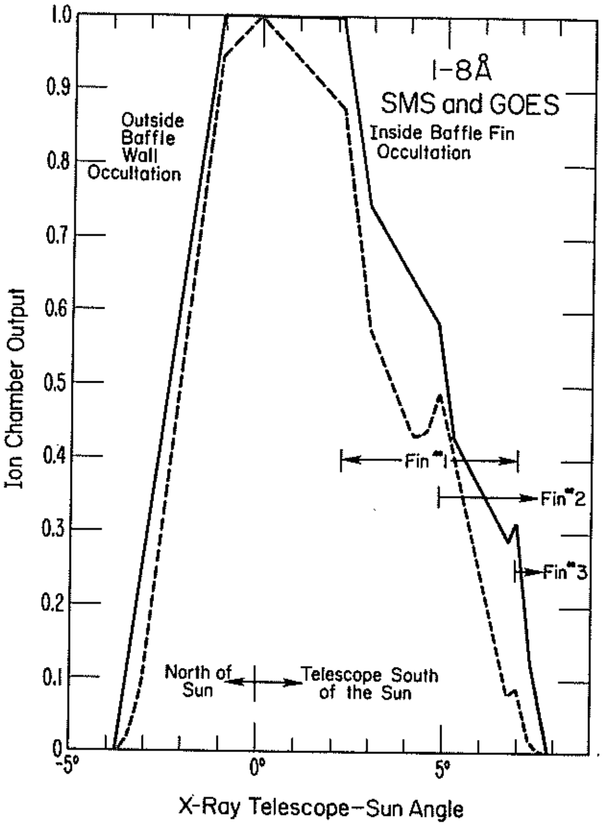

Figure 4.5. Theoretical 1-8 A elevation angle dependence. The solid curve is for wavelengths ≥ 8 A, the dashed curve is for ∿ 1 A. The fins are part of the telescope collimator.

Figure 4.6 shows the theoretical elevation angle response for the $\frac{1}{2}$-4 A ion chamber. The collimator fins located in front of this detector, which are intended to reduce the detector response to energetic particles, cause the sharpness of the elevation angle response at small angles from the Sun. Therefore the $\frac{1}{2}$-4 A ion chamber is the most critical for precise pointing of the telescope as far as keeping the X-ray measurement error very small is concerned. Considering the accuracy at which the X-ray telescope was pointed, the minimum pointing adjustment of 0.25°, and the width of the Sun, we estimate that the telescope was pointed at the main solar X-ray source to within about one-half degree on the average. The $\frac{1}{2}$-4 A measurements should be less in error than being 7% too low for pointing errors less than one-half degree.

4.9. In-Flight Calibrations

The satellite electronics used to measure the current output of the ion chamber are routinely checked by in-flight calibrations. A reference voltage source is used to derive reference input currents for each detector and gain range. Before 1977, in-flight calibrations were made twice daily. Because the

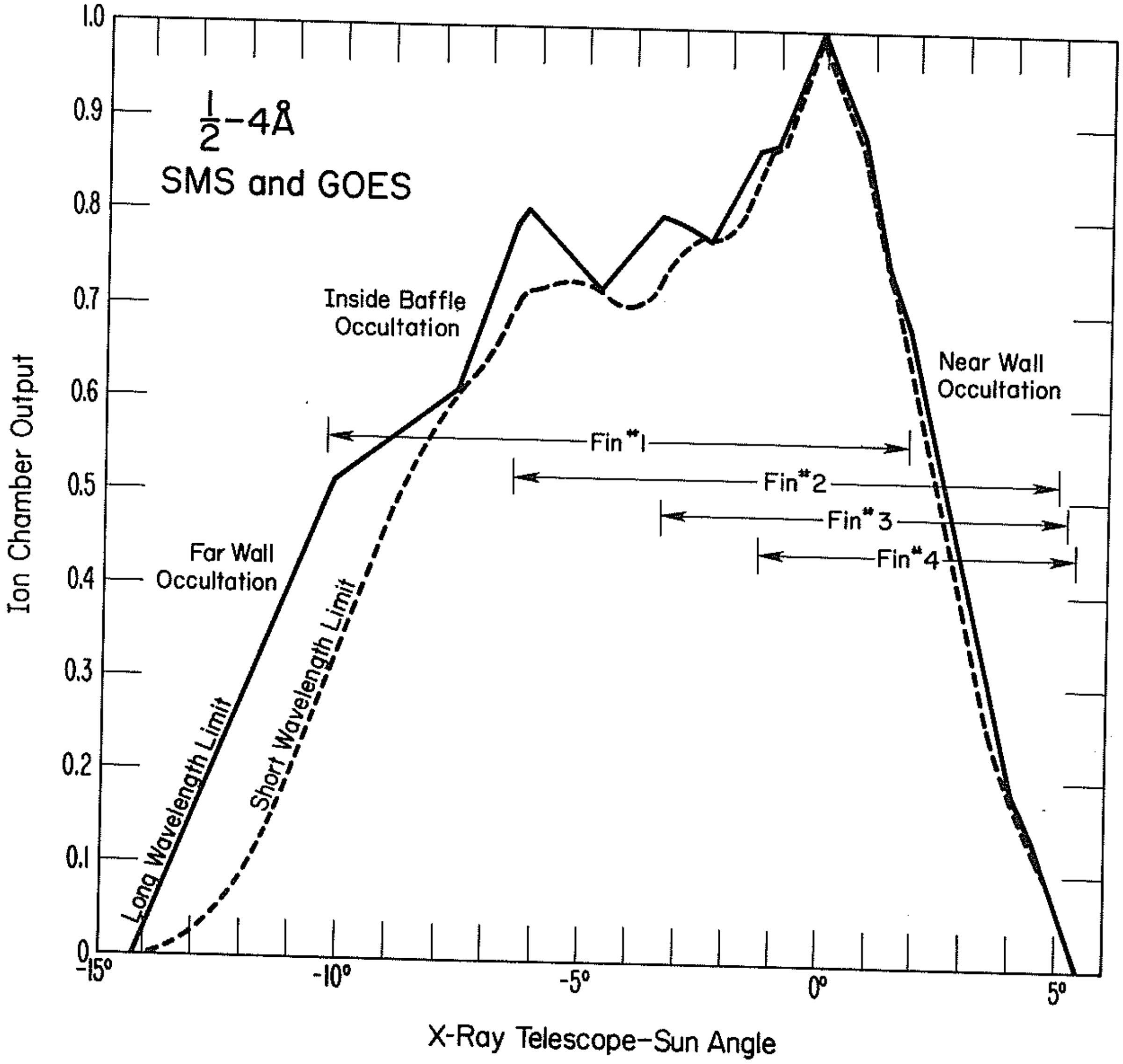

Figure 4.6. Theoretical $\frac{1}{2}$*-4 A elevation angle dependence.*

calibrations have not shown any systematic drifts in electronics gain in several years of operation, the calibrations are now made once per week on Mondays. Table 4.1 lists time averaged calibration results and standard deviations. The day to day variations are usually less than 1%, and the variations over a year are typically less than 2% for the second and third flux ranges and a little higher for the highest and lowest flux intensity ranges of both wavelength channels for all three satellites. These variations are comparable with the intensity resolution. No systematic variation is evident. Therefore no corrections based on the in-flight calibrations were made for the archival data.

Table 4.1. In-Flight Electronics Calibrations

			$\frac{1}{2}$-4 A X-Ray Flux Ranges				1-8 A X-Ray Flux Ranges			
Satellite	Year	Days of Year	Low 1	2	3	High 4	Low 1	2	3	High 4
SMS-1	1975	90-180	9.54±.27*	10.379±.031	7.756±.031	7.91±.31	8.46 ±.70	9.25 ±.77	9.329± .050	9.47 ±.42
		190-270	9.29±.21	9.89 ±.69	7.70 ±.48	8.00±.52	7.95 ±.98	8.23 ±.90	8.73 ±1.04	9.39 ±.81
		280-360	9.27±.27	10.08 ±.45	7.58 ±.26	8.06±.47	8.21 ±.30	8.95 ±.99	8.77 ±1.22	9.44 ±.76
	1976	140-230	9.38±.20	10.313±.034	7.736±.061	7.93±.18	8.22 ±.19	9.44 ±.24	9.319± .089	9.40 ±.31
SMS-2	1975	90-180	8.23±.12	9.082±.047	7.306±.034	7.33±.28	7.85 ±.11	8.863±.025	8.208± .080	8.30 ±.31
		190-270	8.22±.14	8.992±.038	7.25 ±.30	7.16±.22	7.765±.053	8.837±.032	8.07 ± .58	7.84 ±.48
		280-360	7.85±.48	8.928±.042	7.306±.000	7.34±.11	7.56 ±.49	8.718±.143	8.231± .000	8.19 ±.21
	1976	20-140	8.19±.22	9.01 ±.21	7.322±.036	7.42±.26	7.66 ±.25	8.811±.078	8.255± .025	8.39 ±.36
GOES-1	1976	40-50	8.81±.18	9.546±.062	7.395±.023	7.32±.24	7.505±.087	8.278±.049	8.337± .014	8.23 ±.37
		80-90	8.85±.10	9.599±.032	7.377±.015	7.36±.13	7.526±.047	8.328±.021	8.399± .000	8.29 ±.16
		170-180	8.80±.11	9.534±.025	7.420±.016	7.43±.27	7.539±.057	8.396±.013	8.436± .010	8.43 ±.32
		255-265	8.81±.12	9.555±.023	7.389±.023	7.37±.12	7.552±.085	8.343±.020	8.423± .022	8.30 ±.38
		295-305	8.64±.16	9.565±.022	7.423±.028	7.38±.07	7.480±.018	8.296±.021	8.31 ± .29	8.380±.048
		350-360	8.61±.09	9.506±.025	7.411±.020	7.43±.11	7.38 ±.18	8.271±.019	8.399± .000	8.28 ±.36
RANGE UNITS W m^{-2}			x 10^{-8}	x 10^{-7}	x 10^{-6}	x 10^{-5}	x 10^{-7}	x 10^{-6}	x 10^{-5}	x 10^{-4}

The SMS-1 and SMS-2 results above are based on calibrations about every ten days.
The GOES-1 results are based on daily calibrations.

*The first number in all cases gives the average calibration output and the second value gives the standard deviation for the time period involved.

The algorithm used to convert the telemetry output during calibrations to the above effective flux values was the same for all three satellites and did not account for the known differences between the instruments. Therefore the above values should be used only to evaluate the stability of each instrument over the times listed above and should not be used to compare one satellite with another.

4.10. Particle Interference and Background Subtraction

High energy particles induce a background output from the X-ray ion chambers. As the satellite spins, the ion chamber background output may vary when the particle pitch-angle distribution is anisotropic in the conical surface swept by the X-ray telescope. The X-ray instrument measures the background level just prior to observing the Sun and then subtracts that level from the output when viewing the Sun to determine the output from the solar X-rays alone. If the background level is high and varies greatly with satellite spin angle, an error can occur because the pre-Sun background measurement may differ slightly from the particle background when the Sun is viewed. This background subtraction error should be largest when the X-ray flux is low and the particle flux is large and highly anisotropic. Figure 4.7 shows samples of the SMS-2 1-8 A ion chamber background output as a function of satellite spin angle at a time when the solar X-ray flux was very low, too low to measure. This is a case of appreciable spin-modulation of the background.

A telescope collimator and magnetic broom deflector are used to minimize the particle background response. This system appears to have worked quite well because no particle related effects have been identified in the X-ray flux measurements during large particle events recorded by the companion SEMS particle detectors aboard the SMS-GOES satellites. Fortunately, the X-ray flux is usually very high during ionospheric storms when the energetic particle flux is high. For low flux levels, the UV photoelectron problem for SMS-1 (sect. 4.5) greatly exceeds that caused by the particle background. But for SMS-2 and GOES-1, where the UV photoelectron problem was cured (compare figures 4.3 and 4.7), the particle background problem may occasionally be significant.

Several events of unknown origin, but possibly caused by particle interference, occurred in the SMS-2 X-ray measurements in February 1977 (e.g., 1400 UT Feb. 9, 1977) when the solar X-ray flux was very low ($\Phi(1\text{-}8\ \mathrm{A}) \sim 10^{-7}\mathrm{W\ m^{-2}}$ and $\Phi(\frac{1}{2}\text{-}4\ \mathrm{A}) < 10^{-8}\mathrm{W\ m^{-2}}$) and the particle flux was high. The physical processes causing these events are not known. The X-ray flux level decreased to a constant minimum value ($\Phi(1\text{-}8\ \mathrm{A}) \sim 4.3 \times 10^{-9}\mathrm{W\ m^{-2}}$

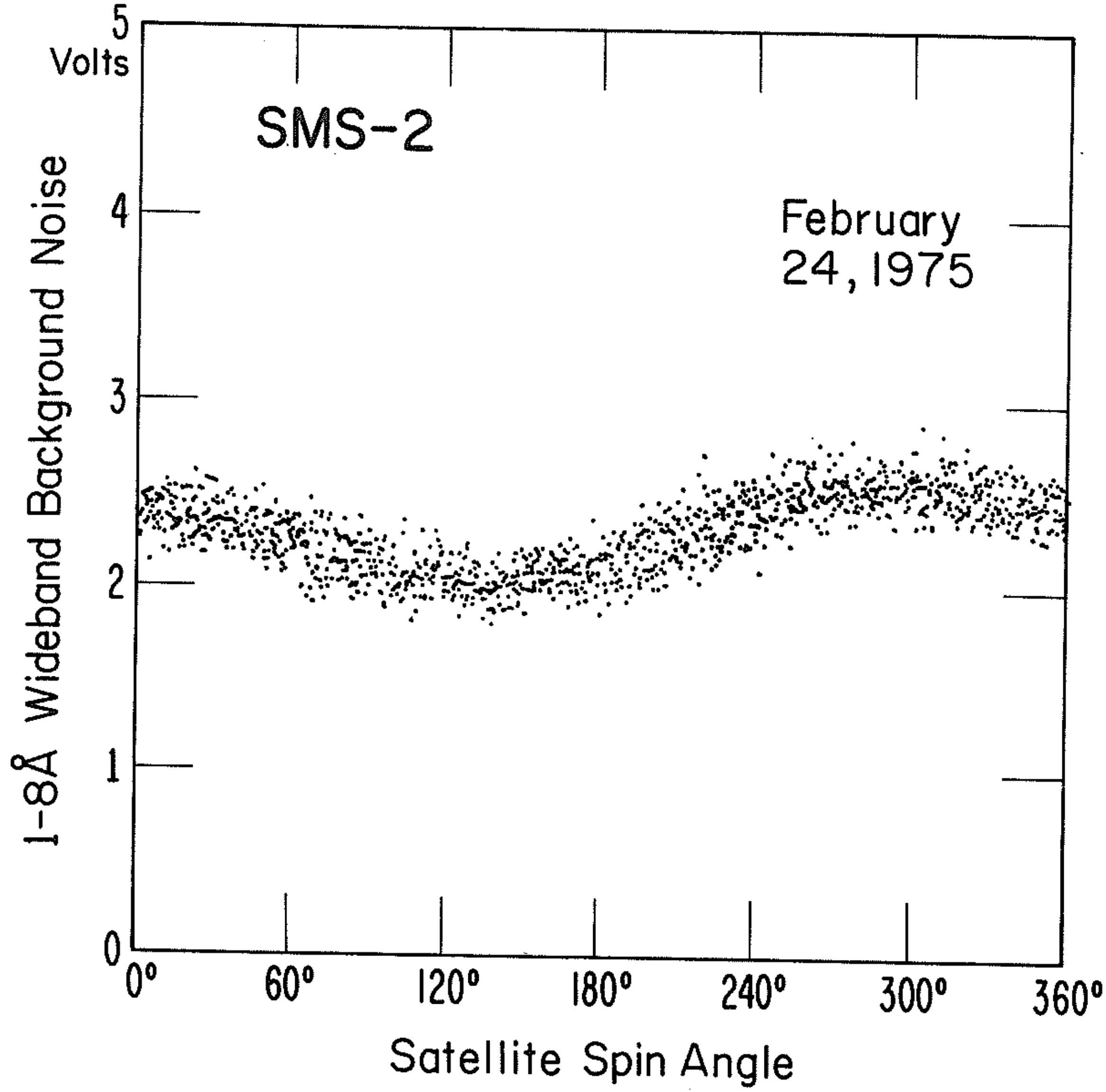

Figure 4.7. Wideband background samples obtained in the dwell mode. Data from a number of satellite spins are superimposed as a function of the satellite spin angle. Data provided by Mr. W. H. Farthing of NASA.

and $\Phi(\frac{1}{2}\text{-}4\ \text{A}) \sim 3.7 \times 10^{-9}\ \text{W m}^{-2}$). The particle flux was enhanced before and after these anomalous "negative" X-ray events, i.e., the time dependence of the particle flux intensity is not similar to that of the "negative" X-ray events. These peculiar events are rare and quite distinct.

5. COMPARISON OF SMS-1, SMS-2, AND GOES-1 X-RAY MEASUREMENTS

Concurrent SMS-1 and SMS-2 data were searched for periods when $\Phi(1\text{-}8\ \text{A}) > 10^{-6}\text{W m}^{-2}$, i.e., when the X-ray flux was strong enough to be terrestrially important. During the sunspot minimum period involved, such X-ray flux levels occurred during solar flares. The flare peak in SMS-1 X-ray flux was used and then flux values ($>10^{-6}\text{W m}^{-2}$) during the rise and decay separated by at least a factor of two in intensity were included. The SMS-2 X-ray flux values for the same times (to within ± 1.5 sec) were used. A comparison of 101 X-ray flux values from 42 solar flares in August 1975, is shown in Figure 5.1. Each point in figure 5.1 is one concurrent sample from both satellites. Linear regression analysis was used to determine the coefficients a and b in the relationship

$$\Phi_{SMS-2} = a\Phi_{SMS-1} + b \qquad (5.1)$$

for a best-fit to these data. The results are given in the first row of Table 5.1. Similar calculations were made to fit a power-law equation to the data. The "a" coefficient of 0.823 is consistent with the SMS-1 $\overline{G}$ having been reduced by times 0.810 from the theoretical calculations whereas the SMS-2 measurements are based only on theoretical calculations, i.e., the coefficient suggests that if similar calibration measurements of $\overline{G}$ for SMS-2 had been made they probably would have been lower than the theoretical values by about the same amount. It is not known for certain whether this difference between the theory and calibration measurements results from an inadequacy in the theory or a systematic error in the calibrations.

Figure 5.1 shows a slight bend in the data trend near the center of the graph. The SMS/GOES measurements achieve both a large dynamic range and high intensity resolution by dividing the overall dynamic range into four ranges, where each range covers about one decade in intensity. The lower or left half of figure 5.1 involves the second intensity range of both satellites and the upper or right half involves the third intensity range. Results are therefore given separately in Table 5.1 for these two intensity ranges.

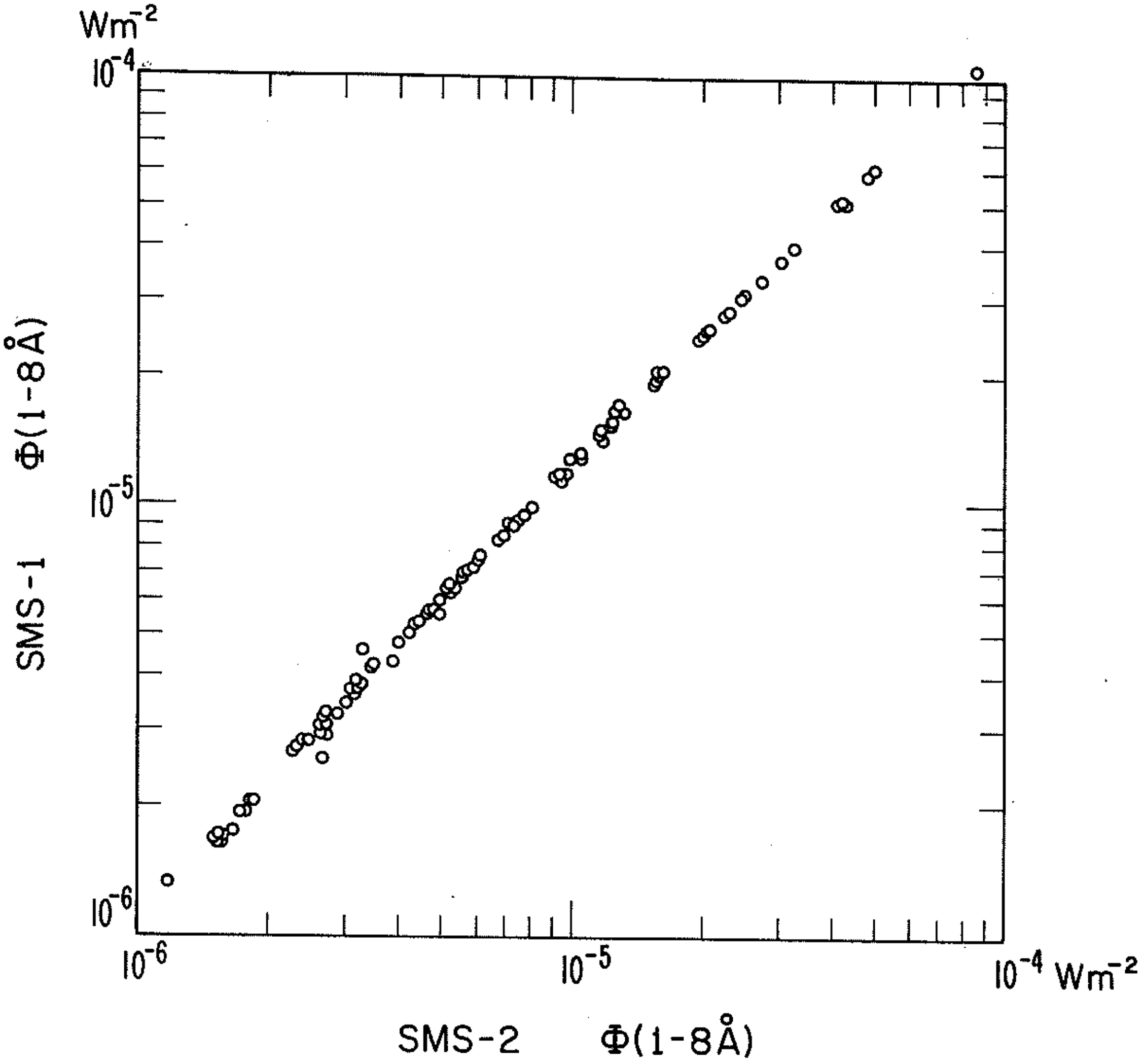

Figure 5.1 Scatter diagram of SMS-1 versus SMS-2 for Φ(1-8 A).

Table 5.1. Linear and Power Law Curve Fits

Satellites		Detector Wavelength Band	Intensity Range	Linear: $\Phi_2 = a\Phi_1 + b$			Power Law: $\Phi_2 = c\Phi_1^d$			Number of Data Pairs
for Φ_1	for Φ_2			a	$b_{W\ m^{-2}}$	Correlation Coefficient	c	d	Correlation Coefficient	
SMS-1	SMS-2	1-8 A	all	0.823	-1.5×10^{-8}	0.9998	0.581	0.969	0.9993	101
SMS-1	SMS-2	1-8 A	$\Phi_1>10^{-5}$W m^{-2}	0.834	-4.8×10^{-7}	0.9999	0.942	1.014	0.9996	37
SMS-1	SMS-2	1-8 A	$\Phi_1<10^{-5}$W m^{-2}	0.792	$+2.3\times10^{-7}$	0.9981	0.373	0.933	0.9977	64
SMS-1	SMS-2	$\frac{1}{2}$-4 A	all	0.940	-5.0×10^{-9}	0.9986	0.872	0.996	0.9984	100
SMS-1	SMS-2	$\frac{1}{2}$-4 A	$\Phi>10^{-6}$W m^{-2}	0.935	$+5.0\times10^{-8}$	0.9979	1.466	1.036	0.9974	42
SMS-1	SMS-2	$\frac{1}{2}$-4 A	$\Phi<10^{-6}$W m^{-2}	0.824	$+4.1\times10^{-8}$	0.9987	0.175	0.886	0.9983	58
SMS-2	GOES-1	1-8 A	all	0.995	-1.7×10^{-7}	0.9997	1.172	1.017	0.9993	62
SMS-2	GOES-1	$\frac{1}{2}$-4 A	all	0.980	$+5.0\times10^{-8}$	0.9992	0.857	0.986	0.9989	77

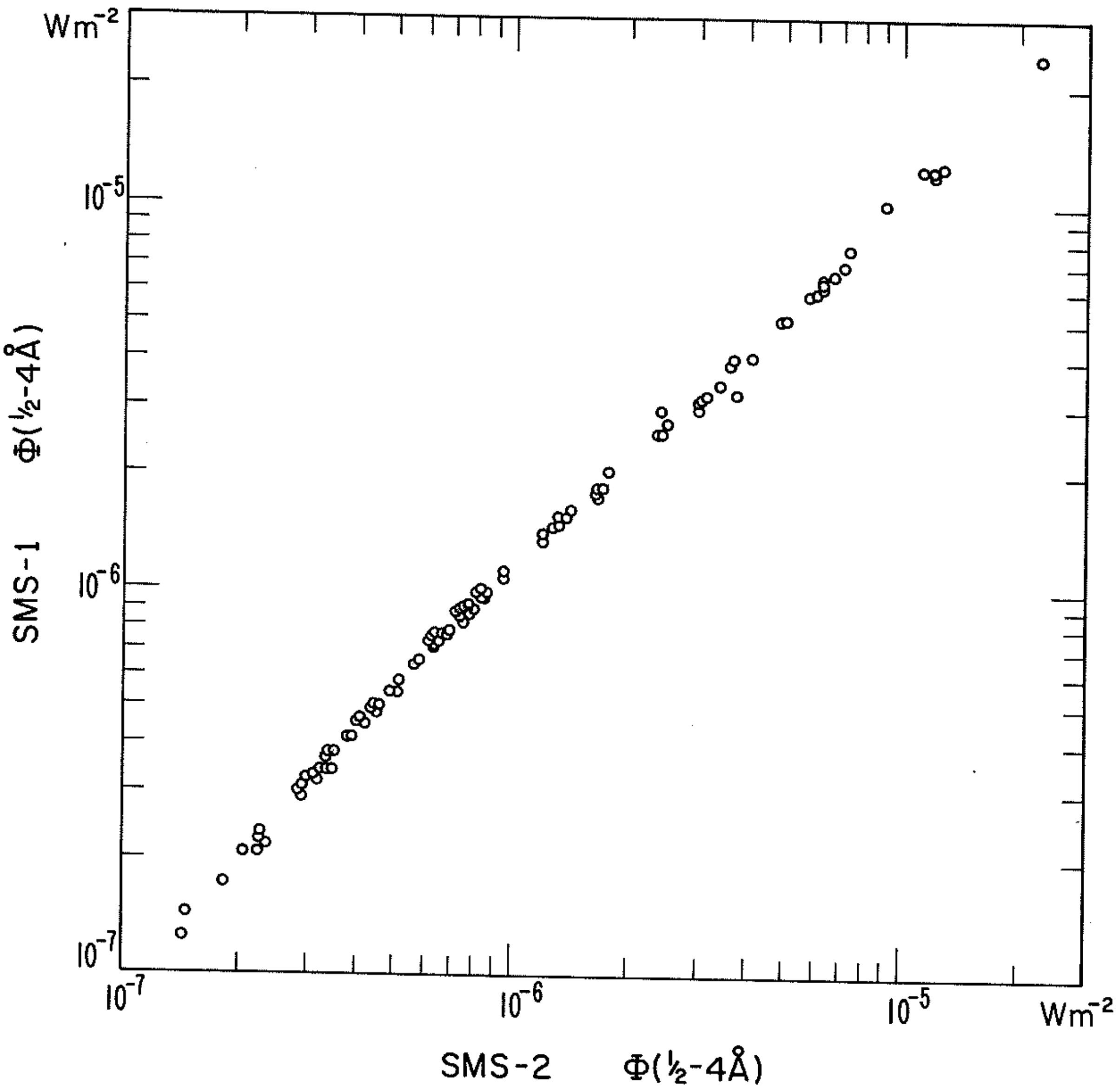

Figure 5.2. Scatter diagram of SMS-1 versus SMS-2 for $\Phi(\frac{1}{2}\text{-}4\ A)$.

Figure 5.2 shows similar results for the $\frac{1}{2}$-4 A range, where the bend in the data near the center of the graph corresponds to the transition from the second to the third intensity range of the $\frac{1}{2}$-4 A instrument. The correlation coefficients should be high because the instruments in these two satellites are so similar. The largest difference between the two satellites occurs at the lowest flux levels in figures 5.1 and 5.2, where the SMS-1 X-ray measurements are too low because of a weak photoelectron current generated by solar ultraviolet radiation. (See sect. 4.5.)

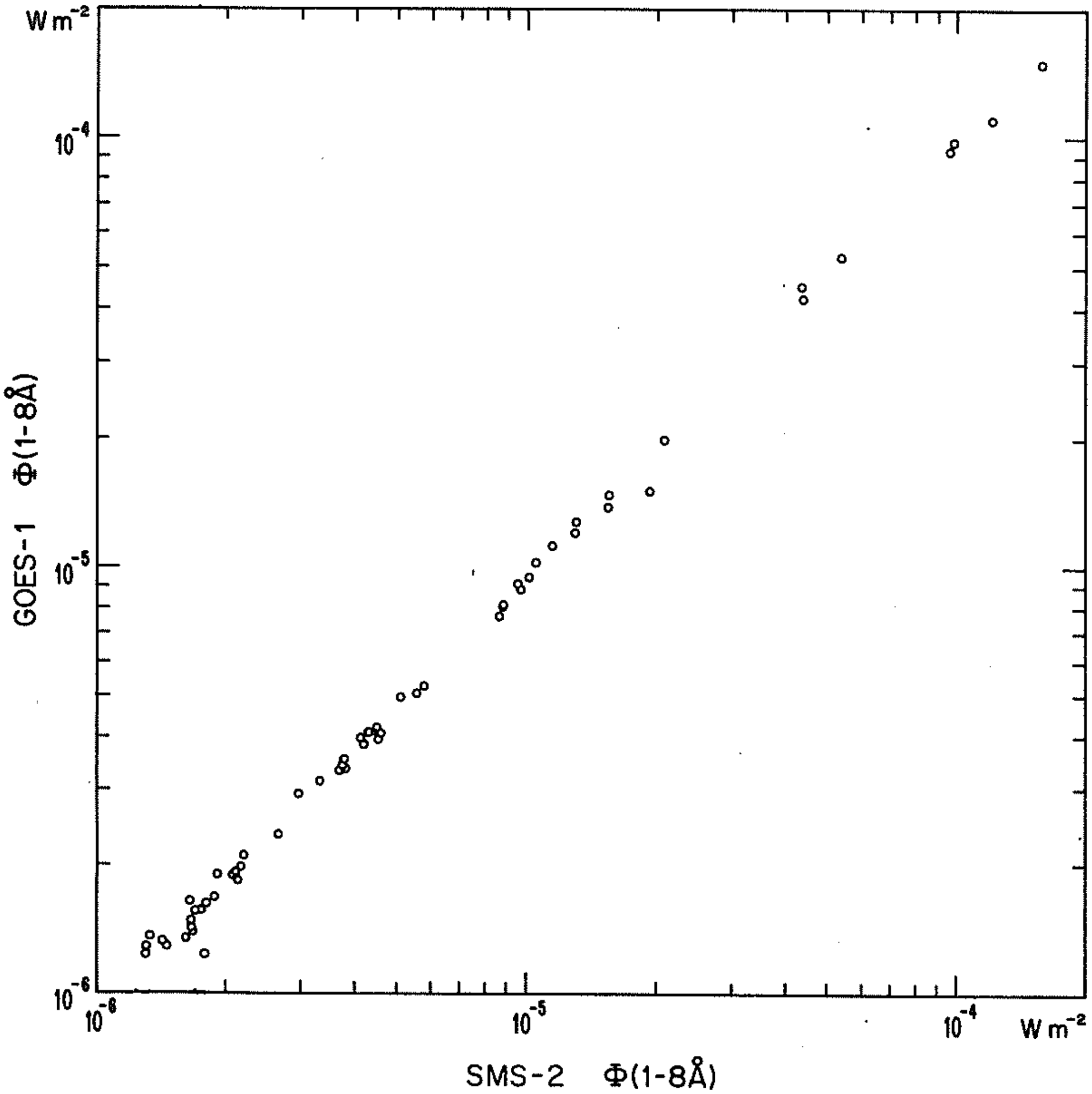

Figure 5.3. Scatter diagram of SMS-2 versus GOES-1 data for Φ*(1-8 Å).*

Similar results are given in Table 5.1 and figures 5.3 and 5.4 for comparison of SMS-2 and GOES-1 X-ray data from 18 solar flares during March 23-27, and April 29-30, 1976. Because the photoelectron problem that occurred in SMS-1 was corrected in both SMS-2 and GOES-1, the intercomparison of the latter data did not show a "bend" at low intensity levels. The SMS-2 and GOES-1 X-ray data usually agree to within several percent. These results are for archive data and include corrections for the effects of the thin filter window added to GOES-1 to block UV radiation. Data provided by the NOAA-SEL-SESC real-time

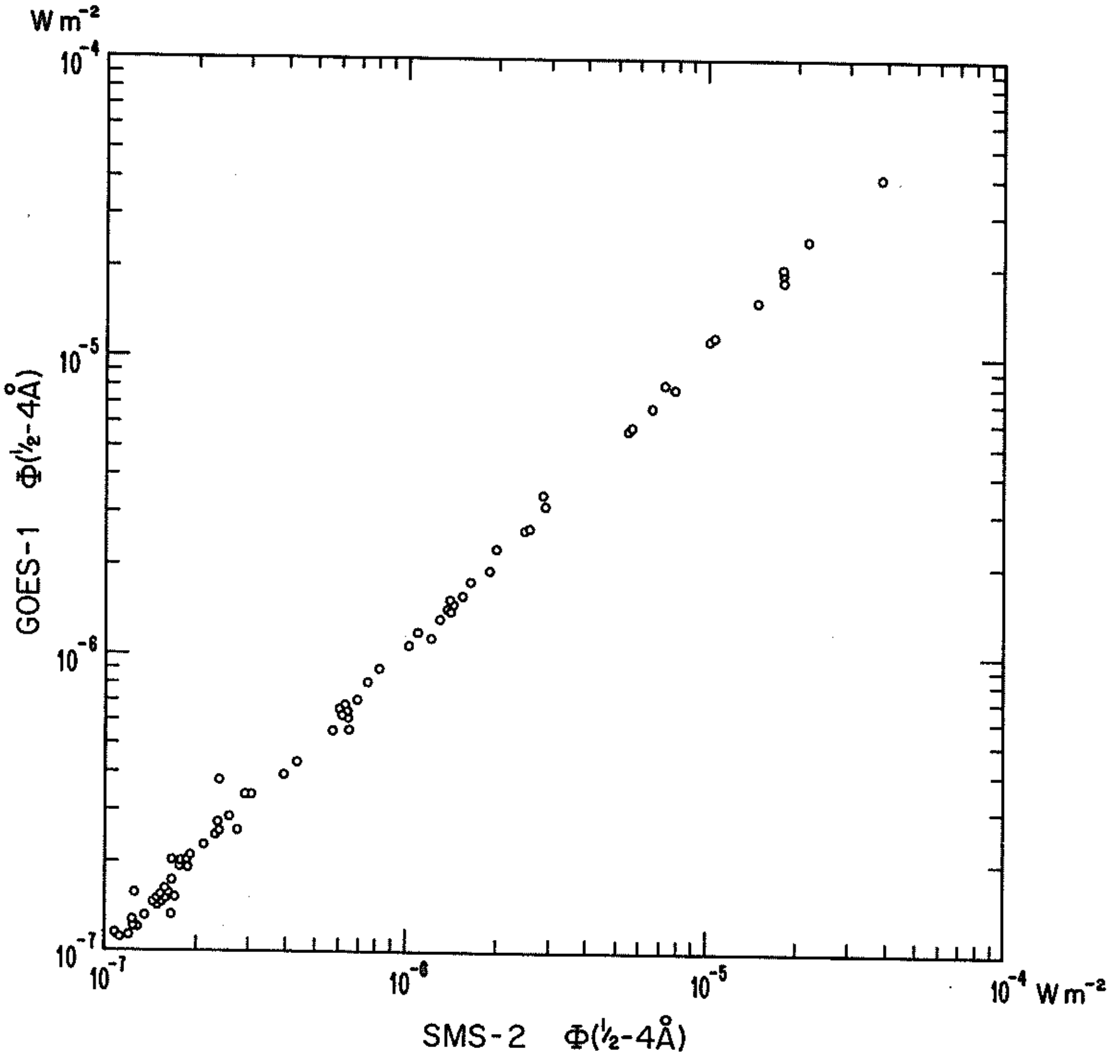

Figure 5.4. Scatter diagram of SMS-2 versus GOES-1 data for $\Phi(\frac{1}{2}\text{-}4\ A)$.

data system prior to April 14, 1977, did not include this correction, which resulted in those preliminary 1-8 A GOES-1 flux values being about 20% too low.

6. SUMMARY OF ERRORS AND CORRECTIONS

The SMS-1, SMS-2, and GOES-1 X-ray data available in real-time from the NOAA-ERL SELDADS system after April 14, 1977, and the archive data discussed in section 7 are based on the standard transfer functions of Table 3.3 and include corrections for the collimator fins in front of the $\frac{1}{2}$-4 A detector and for the thin window added to the GOES-1 detector to block the ultraviolet radiation from shining on the X-ray detector. Corrections for the ultraviolet problem on SMS-1 are not routinely included, but approximate corrections are provided for interested data users in section 4.5. Corrections for the change in spectra as the solar flux decreases below the levels of terrestrial interest to the low quiet-Sun flux levels of sunspot minimum years are not routinely included, but guidelines for making such corrections for the 1-8 A measurements are included in section 3.3. The standard transfer function for the $\frac{1}{2}$-4 A measurements fails before that for 1-8 A as the spectrum softens when the solar flux decreases.

Table 6.1 lists the main estimated errors. The calibration results (Unzicker and Donnelly, 1974) disagree with the theoretical results by about 20%. The SMS-1 transfer functions were normalized to the corresponding laboratory calibration results (sect. 3.1) while the SMS-2 and GOES-1 transfer functions were based solely on theoretical calculations. Comparisons of concurrent SMS-1 and SMS-2 flux measurements showed the SMS-1 1-8 A flux was consistently higher, which probably results from the difference between detector calibration results (SMS-1) and theoretical transfer function values (SMS-2).

The second type of error in Table 6.1 results from the variations in spectral shape (sect. 3.2 and 3.3). The errors listed are much lower than those commonly attributed to this source in the past. We have emphasized picking the standard wavelength averaged transfer function $\overline{G}$ to be appropriate for the high flux levels of interest in terrestrial applications. Lower flux levels involve large errors in the archive flux data based on the standard $\overline{G}$ values, especially for $\frac{1}{2}$-4 A. The ratio of $\Phi(\frac{1}{2}$-4 A$)/\Phi($1-8 A$)$ can be used as a guide to indicate when the standard assumption for $\frac{1}{2}$-4 A is no longer consistent with the observations (sect. 3.3). The observed flux ratios indicate

Table 6.1. Estimated Errors for SMS-GOES X-Ray Measurements

A.	Transfer Function $G(\lambda)$ Accuracy	$\sim \pm 20\%$
B.	Effective Spectral Shape $\overline{G}$ (sect. 3.2, 3.3)	
	1. High 1-8 A flux intensitites:	
	$\Phi(1\text{-}8\ \text{A}) \gtrsim 10^{-6}\,\text{W m}^{-2}$	$\sim \pm 10\%$
	2. High $\frac{1}{2}$-4 A flux intensities:	
	$\Phi(\frac{1}{2}\text{-}4\ \text{A}) \gtrsim 10^{-7}\,\text{W m}^{-2}$	$\sim \pm 15\%$
	(Higher errors may occur during the decay of solar flares)	
C.	SMS-1 Ultraviolet-Photoelectron Effect (see sect. 4.5)	
D.	Telescope Pointing Errors $\lesssim 1/2°$	
	1. 1-8 A	+2% to -0%
	2. $\frac{1}{2}$-4 A	+8% to -0%
E.	Intensity Resolution	
	1. Flux intensity at the high end of a gain range	$\sim 0.3\%$
	2. Flux intensities at the low end of a gain range except for the lowest available gain range.	$\sim 3\%$
F.	Occasional Sources of Error	
	1. Range Switch Transients (sect. 4.1)	
	2. Eclipse Temperature Decreases (sect. 4.3)	$< 3\%$
	3. Isolated Bad Points (sect. 4.7)	

these problems occur below $\Phi(1\text{-}8\ \text{A}) \sim 10^{-6}\,\text{W m}^{-2}$ or $\Phi(\frac{1}{2}\text{-}4\ \text{A}) \sim 10^{-7}\,\text{W m}^{-2}$, except during the decay of solar flares when they can occur at values up to $\Phi(\frac{1}{2}\text{-}4\ \text{A}) \sim 10^{-6}\,\text{W m}^{-2}$.

The relative errors caused by the limit in intensity resolution increases inversely with the flux intensity over each gain range. The three highest gain ranges each involve about one decade in intensity resulting in the values given in Table 6.1. The lowest gain range extends to flux intensities lower than one-tenth the maximum value of the range, so the relative error caused by the limit in intensity resolution is quite large at the low flux end of the lowest flux range.

Considering all errors combined, for flux levels of terrestrial significance, the overall error for 1-8 A measurements should be about ±40%. For the rise and maximum phases of solar flares, the $\frac{1}{2}$-4 A flux should be accurate to about ±50%.

7. ARCHIVE DATA

The SMS and GOES X-ray data since July 1, 1974, are archived in World Data Center for Solar Terrestrial Physics A, NOAA Environmental Data Service, Boulder, Colorado 80302. Copies are available at the cost of processing expenses. The archived data are in two forms: magnetic tapes of digital data for computer processing and microfilm semilog graphs. Figure 7.1 shows one microfilm frame. The graphs cover one hour of data, starting at the hour listed in the upper right hand corner. The satellite involved is listed at the upper left. The day number of the year, the year, the month, and the day of the month appear as numbers along the top of the graph. Each X-ray measurement is plotted in watts m^{-2} as a point, usually about every three seconds. Normally, the points are so close together that they form a continuous curve. Two range switching spikes are evident in each X-ray channel during the rise of the class X5 solar flare shown in the figure. Table 7-1 describes the archive magnetic tapes of X-ray data. The X-ray data are usually three seconds apart in time except when "missing points" (see sect. 4.6) occur or when the original recording of data tapes has malfunctioned, e.g., because of "crashes" or failure of minicomputers. Dwell mode data also are excluded from the archive data. Data are "flagged" to mark occasions when the data are not normal. Table 7.2 explains the flag code. Any of the four flags may be set in a particular flag word. The single-point correction flag is set when the correction is made (see sect. 4.7). The single-point flux given in the archive data is the average of the two adjacent flux values. The flag does not indicate whether the correction was made in the $\frac{1}{2}$-4 A data, 1-8 A data, or both, but this can be determined by comparing the flagged point with the adjacent flux values. The first point after the X-ray instrument has changed gain ranges on either channel is flagged as an aid to identify these points (see sect. 4.1). The flag does not identify which channel is involved, but that is evident from the data. The next four or so 3-sec samples are also affected by the range change but are not flagged. These data are not corrected in the archive data tapes but are simply marked with the flag. The eclipse flag was set whenever the satellite S-band telemetry transmitter was turned off, which is an early step in preparing the satellite to go into the eclipse. The range-change, calibration, and eclipse flags are generated from the original data tapes using data not present in the

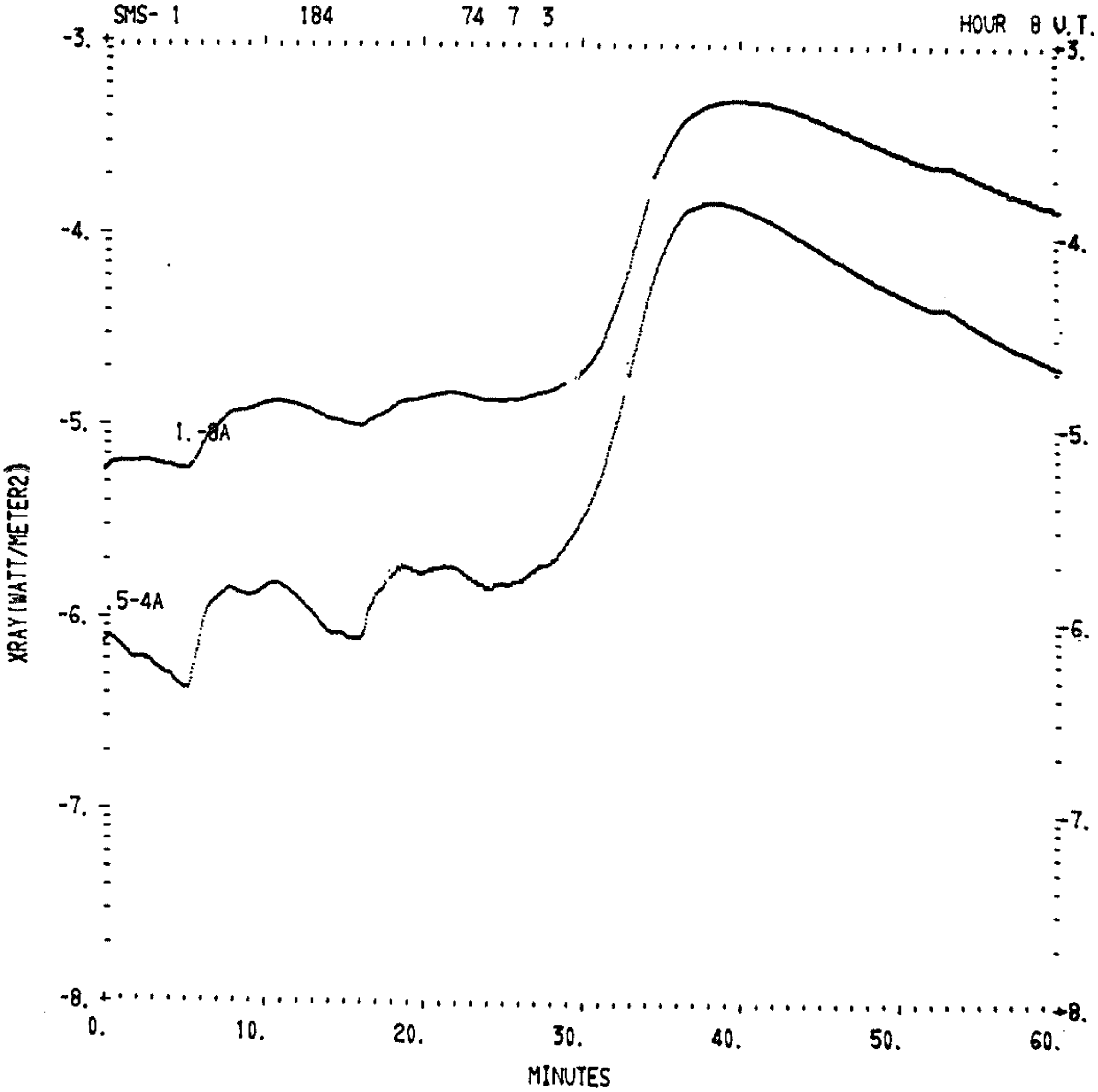

Figure 7.1. An example of the graphs of X-ray data from the archive microfilm.

Table 7.1. Record Structure of SMS X-Ray Archive Tapes

A. RECORD 1: KRONOS 2.1 LABEL

B. DATA RECORD 1 -- 512 WORD, GENERAL INFORMATION

WORD:	NUMBER
1-3	DATA TYPE
4	SATELLITE ID (1=SMS-1, 2=SMS-2, 3=GOES-1)
5	YEAR
6	MONTH
7-37	SATELLITE POSITION
38-62	FLAG CODE INFORMATION
63-512	UNUSED

C. DATA RECORD 2 to N

WORD:		
1-12	AVERAGES WITHIN 5 MINUTE INTERVALS	
13-512	X-RAY DATA IN 4-WORD GROUPS	
	1	SECONDS OF YEAR
	2	1-8 A X-ray flux in W m^{-2}
	3	$\frac{1}{2}$-4 A X-ray flux in W m^{-2}
	4	FLAG

Table 7.2 X-Ray Archive Data Flag Code

Least significant four flag bits.

0000 = no flag

0001 = corrected single point error

0010 = calibration data

0100 = switch in X-ray instrument range

1000 = eclipse of the Sun by the Earth

archive data tapes. Similarly, other housekeeping data are excluded from the archive data tape, for example, data on the temperature of the ion chambers, the temperature of the electronics of the X-ray instrument, and the angle between the X-ray telescope axis and the plane perpendicular to the satellite spin axis. These data are excluded because they are not very useful to scientists using the SMS/GOES solar X-ray measurements.

8. ACKNOWLEDGMENTS

The basic concepts of the SMS and GOES X-ray detector system were developed and demonstrated in a joint study by Bob Kreplin of NRL and Dick Grubb of NOAA. NRL also helped in the calibration measurements for SMS-1. The detailed design of the final X-ray instruments was done by Marion Rinehart of Ford Aerospace and Communications Corporation (formerly Philco Ford) and Terrance Sheridan of Keithley Instruments, Inc. The ion chambers were built by Reuter Stokes, Inc. Also deeply involved were Don Steele, Don McMorrow and Bill Gilliland of FACC and Niel Kacmarcik of Keithly Instruments, Inc. The SMS/GOES program is a joint NASA and NOAA program. The satellites are built under the direction of the SMS/GOES project at NASA Goddard Space Flight Center, launched by NASA, and operated by the NOAA National Environmental Satellite Service. We wish to thank Harry Farthing of NASA Goddard Space Flight Center for his help in post launch tests of satellites and experiments. We thank Dave Bouwer and Jonathon Thron for the data comparisons in section 5. We thank Gregg Merrill and Mike Gallucci of NOAA/SEL for their computer programming help. Finally, we thank the extensive help of Charles Hornbach, Dean Schroeder, Earl Berger, and other members of the NOAA/SEL Real-Time Data Group for their extensive work operating and programming the telemetry receiving system and real-time data processing system that generated the data tapes that are the source for the archive X-ray data tapes. Much of the analysis of the quality of the SMS and GOES X-ray data was based on data obtained from real-time data processing systems. There are scores of people in NOAA NESS contributing to the operation of the X-ray instruments. Nearly all of them work for the following organizations:

Satellite Operations Control Center
Office of Operations
NOAA/NESS
Suitland, Maryland 20233

Wallops Command and Data Acquisition Station
Office of Operations
NOAA/NESS
Wallops Island, Virginia 23337

In particular, we wish to thank Mr. Robert J. Went of the Satellite Operations Control Center for help with our special requests.

9. REFERENCES

Culhane, J. L., A. P. Willmore, K. A. Pounds and P. W. Sanford (1964), Variability of the Solar X-Ray Spectrum below 15 A, Space Research 4, 741-758.

Culhane, J. L., P. W. Sanford, M. L. Shaw, K. F. H. Phillips, A. P. Willmore, P. F. Bowen, K. A. Pounds, and D. G. Smith (1969), A study of the Solar Soft X-Ray Spectrum, Mon. Not. R. Astron. Soc., 145, 435-455.

Donnelly, R. F. (1968), Early Detection of a Solar Flare: A Study of X-Ray, Extreme Ultraviolet, H-Alpha, and Solar Radio Emission from Solar Flares, ESSA Tech. Rept. ERL 81-SDL 2, U.S. Government Printing Office, Washington, DC 20402.

Doschek, G. A. (1972), The Solar Flare Plasma: Observation and Interpretation, Space Sci. Rev., 13, 765-821.

Grubb, R. N. (1975), The SMS/GOES Space Environment Monitor Subsystem, NOAA Tech. Memo ERL SEL-42, NOAA Space Environment Laboratory, Boulder, CO 80302.

Kreplin, R. W., T. A. Chubb and H. Friedman (1962), X-Ray and Lyman-Alpha Emission from the Sun as Measured from the NRL SR-1 Satellite, J. Geophys. Res., 67, 2231-2253.

Kreplin, R. W., K. P. Dere, D. M. Horan and J. F. Meekins (1976), The Solar Spectral Irradiance Below 10A, The Solar Output and Its Variation, ed. O. R. White, J. A. Eddy and D. Heath, U. Colo. Press.

Mewe, R. (1972), Calculated Solar X-Radiation from 1 to 60A, Solar Phys., 22, 459-491.

Neupert, W. M. (1971), Solar Flare X-Ray Spectra, Phil. Trans. Roy. Soc. London, Ser. A, 270, 143-155.

Neupert, W. M., M. Swartz, and S. O. Kastner (1973), Solar Flare Line Emission Between 6A and 25A, Solar Phys. 31, 171-195.

Pounds, K. A. (1970), The Solar X-Radiation Below 25A, Ann. Geophys., 26, 555-565.

Tucker, W. H. and M. Koren (1971), Radiation for a High-Temperature, Low-Density Plasma: The X-Ray Spectrum of the Solar Corona, Astrophys. J., 168, 283-311.

Unzicker, A. and R. F. Donnelly (1974), Calibration of X-Ray Ion Chambers for the Space Environment Monitoring System, NOAA Tech. Rept. ERL 310-SEL 31, U.S. Government Printing Office, Washington, DC 20402.

Vaiana, G. S., A. S. Krieger, A. F. Timothy (1973), Identification and Analysis of Structures in the Corona from X-Ray Photography, Solar Phys., 32, 81-116.

Walker, Jr., A. B. C., H. R. Rugge, and Kay Weiss (1974), Relative Coronal Abundances Derived from X-Ray Observations. I. Sodium, Magnesium, Aluminum, Silicon, Sulfur and Argon, Astrophys. J., 188, 423-440.

Wende, C. D. (1971), The Normalization of Solar X-Ray Data from Many Experiments, NASA X-601-71-166, NASA Goddard Space Flight Center, Greenbelt, Maryland, 1971. See also Solar Phys., 22, 492-502.

Williams, D. J. (1976), SELDADS: An Operational Real-Time Solar-Terrestrial Environment Monitoring System, NOAA Tech. Rept. ERL 352-SEL 37, U.S. Department of Commerce, National Oceanic and Atmospheric Administration, Environmental Research Laboratories, Boulder, Colorado 80302

☆ U.S. Government Printing Office: 1977-777-045/1261 Region 8